Czech Technical University in Prague
Faculty of Nuclear Sciences and Physical Engineering
Department of Physics

MASTER THESIS

Application of antiprotons for radiotherapy

(Studium využití antiprotonů pro radioterapii)

Praha, 2006 **Hedvika Toncrová**

Název práce:	**Studium využití antiprotonů pro radioterapii**
Autor:	Toncrová Hedvika
Obor:	Matematické inženýrství
Druh práce:	Diplomová práce
Vedoucí práce:	RNDr. Vojtěch Petráček, CSc., Katedra fyziky, Fakulta jaderná a fyzikálně inženýrská, České vysoké učení technické v Praze
Konzultant:	Dr.Michael Doser, CERN, Švýcarsko

Prohlašuji, že jsem svou diplomovou práci vypracovala samostatně a použila jsem pouze podklady (literaturu, projekty, SW atd.) uvedené v přiloženém seznamu.

Nemám závažný důvod proti užití tohoto školního díla ve smyslu § 60 Zákona č.121/2000 Sb. , o právu autorském, o právech souvisejících s právem autorským a o změně některých zákonů (autorský zákon).

I declare that I have written this diploma thesis independently using the listed references. I agree with using this diploma thesis.

V Praze dne _____ _____

Hedvika Toncrová

Acknowledgement

I would like to express my gratitude to all those who gave me the possibility to complete this thesis. I want to thank my CERN supervisor Dr. Michael Doser, for involving me in the project and helping me throughout the initial phases of the work. The summer at CERN was an unforgettable period of my life.

I am deeply grateful to my supervisor, RNDr. Vojtěch Petráček, for his detailed and constructive comments, and for his important support throughout this work.

I also wish to thank Jamie (super damn cool) Tattersall, who looked closely at the final version of the thesis for English style and grammar, correcting both and offering suggestions for improvement.

Especially, I would like to give my special thanks to my parents whose endless patience and love enabled me to complete this work.

Abstrakt

Využití antiprotonů pro radioterapii představuje alternativu k tradičním radioterapeutickým metodám a zdá se že je i v mnoha ohledech výhodnější. Výsledky prvních experimentů totiž naznačují že jejich biologická účinnost je až čtyřikrát vyšší než biologická účinnost protonů, v současné době jedněch z nejúčinějších částic používaných v radioterapii. Dalším potencialním přínosem antiprotonů je možnost zobrazit rozložení míst anihilací v prostoru pomocí vysokoenergetických částic vyzářených z místa anihilace. V ideálním případě by tato zobrazovací metoda byla použita před samotnou terapií k ověření terapeutického plánu a poté ke kontrole průběhu vlastního ozařování.

Navržený terapeutický plán by mohl být ověřen ozářením pacienta zkušebním paprskem o nízké intenzitě, který by byl následován plnou dávkou. V průběhu plného ozařování může zobrazovací zařízení sloužit pro zpětnou vazbu. To by mohlo představovat velkou výhodu této metody, zejména pro nádory uložené v blízkosti citlivých oblastí. První experiment, který zkoumal možnosti zobrazování byl proveden na antiprotonovém dekcelrátoru v CERNu a dalši budou v blízké době následovat.

První kapitoly této práce jsou věnovány historii radioterapie a fyzikálním principům, které jsou při ní využívány. Část je tvořena rychlým přehledem experimentů, které zkoumaly interakci antiprotonů s biologickými tkáněmi. Samostatná kapitola je věnována výše zmíněnému experimentu, který testoval možnosti zobrazení cílového objemu záření. Bohužel během experimentu došlo k selhání některého z přístrojů a tak jsou data z experimentu neúplná a tudíž nemohla byt analyzována. Je však ukazáno že velikost cílového objemu může být rekonstuována jen velmi přibližně s použitým experimentálním uspořádáním. Proto je největší část této práce zaměřena na návrh vylepšeného uspořádání, které je citlivější k parametrům prostorového rozložení anihilací. Jsou navržena dvě experimentální uspořádání a jejich chování je simulováno. Program, který z naměřených hodnot rekonstruuje původní distribuci je popsán a výsledky představeny. Navržená uspořádání jsou velmi jednoduchá aby se ulehčila jejich instalace v prostorách antiprotonového dekcelerátoru. Nicméně rekonstrukce je poměrně přesná a tak by základní myšlenka mohla najít uplatnění i v budoucích klinických aplikacích.

Klíčová slova: antiprotony, radioterapie.

Abstract

Antiprotons offer an alternative to established radiotherapeutic methods. Initial trial experiments indicates that the biological efficiency of antiprotons is up to four times higher than that of protons, currently one of the most efficient particles used in radiotherapy. Another potential benefit of antiprotons is the possibility to image the stopping distribution using the high energy particles that emanate from the annihilation vertex. Optimally the imaging would be used at first to confirm a therapy plan and later to control the course of irradiation.

A therapy plan can be confirmed with a low intensity beam before the patient is irradiated with a therapeutical dose. In the course of the irradiation the imaging device can serve as a control system. This could be a great advantage, especially for tumors located close to sensitive areas. A first experiment to test the possibilities of the imaging was carried out at the AD facility at CERN and other experiments will follow in forthcoming beam time.

The first chapters of this thesis are devoted to a history of radiotherapy and its physical principles. A part of it is a quick review of important experiments testing the interaction of antiprotons with biological tissues. The next chapter describes the experiment which tested the real time imaging. Unfortunately during the experiment a failure of technical devices caused the data acquired from the experiment to be incomplete and it cannot be used for analysis. It is shown that only the bulk properties of the stopping distribution could be reconstructed with the experimental design used. Therefore a main part of this thesis refers to a proposal for an improved experiment which is more sensitive to the parameters of the stopping distribution. Two experimental designs are proposed and its performance simulated. The program that reconstructs the stopping distribution from the acquired data is described and its results presented. The designs are very simple in order to facilitate the installation of the experiment in the area of the AD. The reconstruction, however is fairly precise and therefore the main idea of the design could be used in clinical applications.

Keywords: antiprotons, radiotherapy.

Contents

List of Figures

List of Tables

Chapter 1

Introduction

Radiotherapy is a hundred year old method of curing cancer and ranks among the most successful. For decades after its discovery it was stigmatized by the lack of understanding of the physical principles underlying the interaction of the radiation with matter. Unfortunately, for a long time after the clarification of the physical phenomena radiotherapy was still being administered based on empirical estimates. A radical change only came with the invention of computer tomography (CT), which facilitated precise treatment planning and thus dramatically reduced side effects.

Since that moment radiotherapy research has concentrated on improving the established methods and on discovering and testing new methods. The purpose of these methods is to kill all the cancer cells of a well defined tumor whilst sparing the normal tissue that surrounds it. At the disposal of the research is the detailed knowledge of the particle physics and numerous experimental facilities. This leads to quick development and this field of medicine has gathered great success.

Currently there are several established radiotherapy methods that are used worldwide and a few methods that still have to convince physicians and patients to accept them. The historical overview with short descriptions of a few of the most commonly used methods is devoted to the first chapter. This thesis deals with a potential alternative which is radiotherapy using antiprotons. Preliminary results hint that this method could bring another significant improvement. Antiprotons, compared to other particles, do not deliver only their kinetic energy, but deposit additional energy that is released during the annihilation in the close vicinity of the annihilation vertex. Despite the amount of energy being small, it is deposited with high biological efficiency.

Another potential benefit of the annihilations is that the high energy annihilation products escape the body and can be detected afterwards. If the particles can

be traced backwards and the annihilation vertex localized, the three dimensional image of the annihilation volume can be obtained. A therapy plan can therefore be confirmed with a low intensity beam before the patient is irradiated with a therapeutical dose. In the course of the irradiation the imaging device can serve as a control system. This could be a great advantage, especially for tumors that are located close to sensitive areas.

The real time imaging is a main subject of the thesis. In chapter 4 the first experiment is described, which tested the real-time imaging capabilities. The analysis of this experiment is also a part of that chapter. The experiment did not go as well as expected and therefore it is advisable that it is repeated. An improved design for the new experimental is proposed in the chapter 5. The original experiment as well as the experiment with the improved detector layout were simulated using the Monte Carlo simulation toolkit GEANT4. The chapter 3 addresses the principles of beam therapy, the process of annihilation and the way this process is simulated in GEANT4.

Chapter 2

Radiotherapy

Radiation therapy had its beginning as a treatment of cancer soon after the discovery of X-rays by Roentgen in 1895, radioactivity by Becquerel (1896) and radium by Marie and Pierre Curie (1899). The first therapy trial was carried out in 1895 by Emil Grubbe. However the first real cancer cure using X -Rays is reported in the literature by prof.Freund in 1899.

The first decades after the discovery of X-rays are viewed as the "Dark Ages" in the evolution of radiation therapy. Surgeons administered the treatment with little understanding or knowledge of the physical nature and biological effects of radiation. Many complications occurred after treatment with radiation due to the destruction of the normal tissues. The literature of this decade has many examples of tissue necrosis, infection, and death as a result of treatment. The rate of tumor recurrence was also reported as high.

In 1920's a big effort was made investigating radiation and its interaction with biological tissues. It was later discovered that radiation therapy worked by damaging the DNA of cells. The damage is caused by the passage of particles through cells, directly or indirectly ionizing the atoms which make up the DNA chain. A dosage unit and the use of smaller daily doses of radiation rather than a single massive dose were introduced. The physicists also quickly realized that in order to spare the healthy tissue in front of the tumor, the energy of the photons for deep seated tumors has to be increased. The X-rays were replaced with high energy γ rays.

There was still a major problem left though. This was that the tumor target could often not be well defined within a patient. To compensate, larger volumes than necessary were irradiated, which further increased the side effects. A major breakthrough was the invention of computer tomography (CT). It became an essential tool for treatment planning.

With improved planning development focused on new methods that could target the treatment more precisely. Some scientists put their effort on improving a conformal photon therapy and others started to look for other particles that could be used instead of photons. The use of ions and protons came into focus.

A photon deposits most of its energy in the body at a depth ranging from 3 mm to 5 cm from the surface, depending on the energy of the photon. Efforts to improve photon therapy lead to the use of multiple beams at the same time. Every beam deposits its maximum energy close to the surface, however the various lesser, post-peak doses add up in the target volume. The additive dose is higher then that received by normal tissue. Photon plans are designed to build up a sufficient dose within the target while still keeping the normal-tissue dose low enough to minimize damage.

The use of heavy charged particles like protons or heavier ions is advantageous because the profile of the deposited energy peaks is at the end of the range of the charged particle rather than near the surface as is the case with photon based therapy. The biological effectiveness of a radiation method depends above all on the density of ionization or LET (linear energy transfer) of the particle as it moves through the body, which depends on the charge and velocity of the ion. Protons as well as heavier ions show a steep increase in ionization density towards the end of their particle range.

The conventional photon or electron beams cannot build up a maximum of energy deposition or even stop at any desired depth within a patient. This is achievable using heavy charged particles and thus enables the treatment of tumors in very sensitive zones. This supported the development of proton and heavy ion therapy. Presently there are many facilities that successfully use protons or heavier ions.

A potential improvement of radiation therapy is expected to be achieved with the use of antiprotons and this is now being tested. Antiprotons are biologically more effective than all of the particles tested so far. Their slow down in a very similar way to protons. However when they stop, they annihilate producing a variety of low and high-energy particles. The enhanced biological effectiveness stems from the recoils and fragments that come from annihilation events where one of the pions interacts with the nucleus to cause nuclear excitation with subsequent breakup. These heavy fragments and recoils have a short range and deposit all their energy in a localized region around the annihilation vertex. The higher energy neutrons emitted in the annihilation process have intermediate ranges and result in a diffuse neutron radiation background centered on the tumor, but extending beyond the

targeted region. Similarly, the higher energy emitted particles such as pions will produce some background radiation beyond the immediate region of annihilation. The high-energy pions, muons, and gammas that leave the body have the additional potential to be used for imaging.

2.1 Studies of antiprotons for radiotherapy

Gray and Kalogeropoulos (Gray and Kalogeropoulos, 1984) estimated that in the reactions following the annihilation of an antiproton t[illegible]e will be deposited an additional energy of 30 MeV in the close vicinity of the annihilation vertex. This is a small amount compared to the total annihilation energy of 1.88 GeV, but by being delivered in the form of high LET radiation it has a significant enhancement effect for biological purposes.

The experiment AD-4/ACE (Antiproton Cell Experiment) was the first to directly measure the biological effect of antiproton annihilation (Holzscheiter et al., 2004). The first data was taken in 2003 and was performed on the AD (Antiproton Deccelerator) at CERN. The AD is the only facility in the world that has a low energy, mono-energetic beam of antiprotons able to deliver a biologically meaningful dose at an appropriate dose rate and thus is the only one suitable for this experiment.

In the experiment it was found that the additional energy deposited after the annihilation caused an increase in the "biological dose" in the vicinity of the Bragg peak as predicted. The enhancement of this dose compared to protons was determined and an approximate dose range for meaningful biological exposures established.

The experiment used a beam of 300 MeV/c antiprotons from AD extracted into a biological sample of li[illegible]cells. The cells were embedded in a gelatine kept in a tube of 6 mm in diameter that was placed at the end of DEM beam line. The tube was kept at the temperature of 2 °C, prohibiting any movement of the cells.

The tube was irradiated, then cut into 1 mm slices along the beam axis and cell survival fractions in each slice was determined. The whole experiment was repeated for a variety of doses. A Bragg peak of mono-energetic beam of antiprotons is only 1.5 mm wide at the FWHM value. The method of taking 1 mm thick samples required the width of the peak to be enlarged. This was achieved with a static degrader and the final width was 2.8 mm. The fractions of survived cells in each slice gave a family of survival vs. depth curves (Fig. 2.1).

Deposited energy was also measured by irradiating GAF chromic film placed

both perpendicular to the beam and axially in the beam. A GAF chromic film demonstrates the ionized radiation through a chemical-physical process of polymerization that changes the color of the film in proportion to the quantity of absorbed radiation. A GAF chromic film can be easily positioned in any area inside a phantom and serve for the quantification of the absorbed dose. The axial and lateral dose profiles measured with a GAF chromic film are shown in figure 2.2.

To study the biological effectiveness of antiprotons the term Biological Effective Dose Ratio (BEDR) was defined as the ratio of the biological effects in the entrance channel ("plateau") and the annihilation region ("peak") of an antiproton beam entering a biological target. The introduction of BEDR makes the measurement largely independent of any precise knowledge of absolute dose and facilitates the comparison to protons. The ratio of dose necessary to produce 20% cell survival in the plateau and the peak region ($BEDR_{20\%}$) for antiprotons was found to be of 9.8, compared to 2.5 for protons. This means that antiprotons are about four times more effective than proton, which is a significant improvement. In order to compare

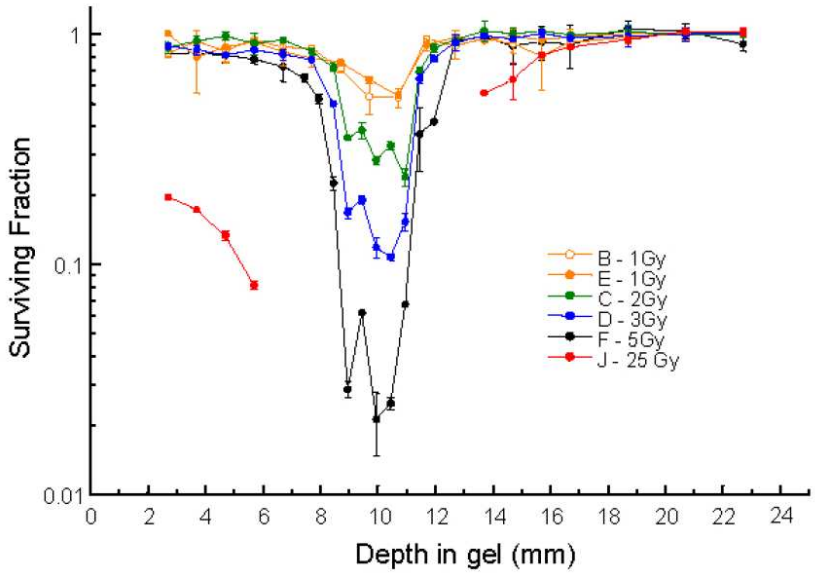

Figure 2.1: Survival of V79 Chinese Hamster cells vs. depth in gelatin irradiated with an antiproton beam of 300 MeV/c momentum. A static degrader was used to introduce an energy spread to the monochromatic beam in order to increase the width of the Bragg peak to about 2 mm. The variation of survival fraction in the peak is an artifact of the structure of this degrader. Source (Holzscheiter, 2004).

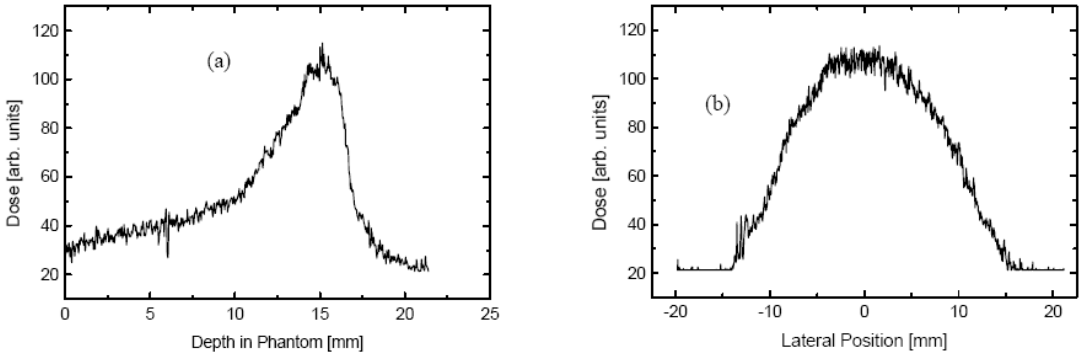

Figure 2.2: (a) Axial and (b) radial profile of the dose deposited in a phantom as measured with GAF chromic film. The lateral width of the beam was 3 cm, the width of the Bragg peak 2.8 mm. Source (Agazaryan et al., 2003).

the data of proton and antiproton experiments, the position of plateau was redefined for protons. It was defined as the slice which is at the same distance from the Bragg peak as was used for the analysis of antiproton experiments. The summary of the results is shown in Fig. 2.3.

In order to understand the significance of the results obtained with antiprotons it is necessary to perform a direct comparison experiment with a beam of protons and heavy ions under the same conditions as with the beam of antiprotons. For a comparison with protons the TRIUMF facility in Canada was chosen. A first round of comparison experiments conducted in 2003 and 2004 there and at CERN showed a significant enhancement of the BEDR for antiprotons compared to protons. For details see (appendix b of status report 2004). For a comparison experiment with carbon ions the GSI facility in Darmstadt, Germany was chosen. This experiment was approved for beam time in 2006 and 2007 and will be conducted in collaboration with the biophysics group of Prof. G. Kraft at GSI.

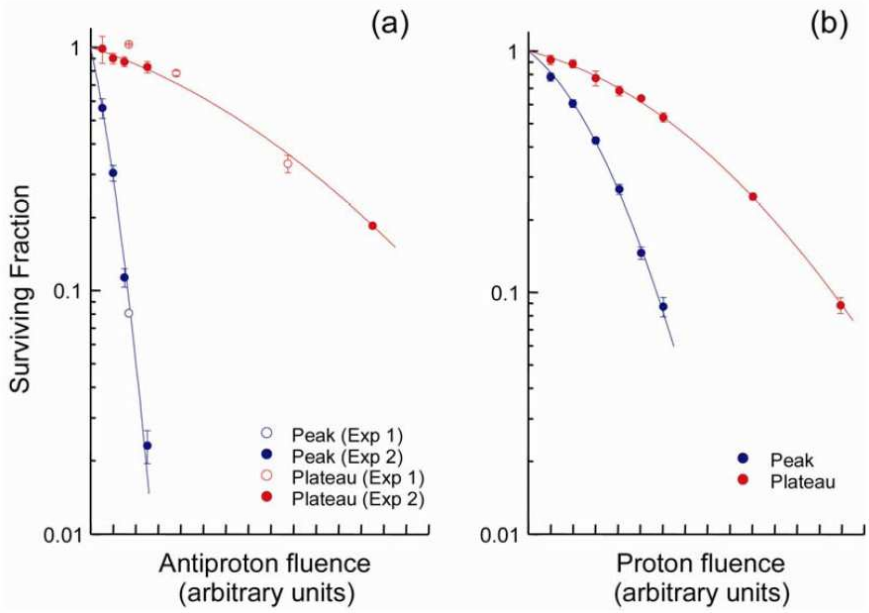

Figure 2.3: Survival for Peak and Plateau regions of V79 Chinese Hamster cells irradiated with an antiproton beam (a) and a proton beam (b) of 50 MeV kinetic energy. The BEDR for 20% survival is 9.8 and 2.5 respectively for the two cases. Source (Holzscheiter, 2005).

2.2 Imaging

From the annihilation of antiprotons a variety of low- and high-energy particles emanates. Whilst the low-energy ones deposit their energy in the vicinity of the annihilation, the high-energy particles leave the body without depositing a significant amount of energy. These particles have the great potential to be used for imaging the stopping distribution of antiprotons in the real time.

An initial low intensity beam could thus be used to confirm that the annihilation "peak" appears in the desired target. Then, after establishing conformity, the beam intensity could be increased to a therapeutic level. The imaging facility could be further used to monitor the course of the therapy and serve like a safety-catch if anything goes wrong. This could be another great benefit of the antiproton therapy, especially for the tumors located close to sensitive areas in the body.

Two types of particles are interesting for imaging: the charged pions (typically 3 per annihilation) and the neutral pions which are converted into high energy γ. If these particles can be detected outside the target in a way that their path can be traced backwards to the annihilation point, a 3-dimensional image of the annihilation

volume can be obtained.

Although not mentioned in the original proposals the real-time imaging soon became a solid part of the ACE experiment. A first prototype experiment designated to test the possibilities of the real-time imaging was performed in November 2005 at AD at CERN by Michael Doser and Petra Riedler.

The analysis of this experiment forms one part of this thesis. The details of the experiment are given, together with the analysis in the chapter 4. However at first I will devote a short chapter to the physical principals of the beam therapy and to the process of annihilation.

Chapter 3

Principles of beam therapy

The main argument for the use of heavy particle beams in therapy is the increase of energy deposition with penetration depth. This phenomena was first described for α particles in a publication by Bragg in 1903 and was confirmed for protons and heavier ions in measurements by Robert Wilson at Berkeley, California, in 1946 (Wilson, 1946). In Fig. 3.1 is the depth dose profile of electromagnetic radiation compared to that of protons and carbon ions.

The slowing down of antiprotons in matter is very similar to that of protons. Within the range of therapeutically relevant energies of several hundred MeV the process of energy loss can be described by the Bethe-Bloch formula.

$$\frac{dE}{dx} = \frac{4\pi e^4 Z_{eff}^3 ZN}{m_e v^2} \ln \frac{2mv^2}{I} + relativistic\, terms \tag{3.1}$$

where $\frac{dE}{dx}$ is the energy loss per length, Z the target atomic number, N the electron density of the target, I the mean ionization potential, m_e and e the mass and charge of the electron, $v = \beta c$ the projectile velocity. Z_{eff} is the effective projectile charge, it can be approximated by the Barkas formula:

$$Z_{eff} = Z(1 - \exp(-125\ \beta Z^{-\frac{2}{3}})) \tag{3.2}$$

Apparently, dominant in the Bethe-Bloch formula (3.8) is the $\frac{1}{v^2}$ and the Z_{eff} dependence. The $\frac{1}{v^2} \approx \frac{1}{E}$ dependence yields an increase in energy loss with decreasing particle energy. The Bragg curve of a beam is much wider than the curve drawn

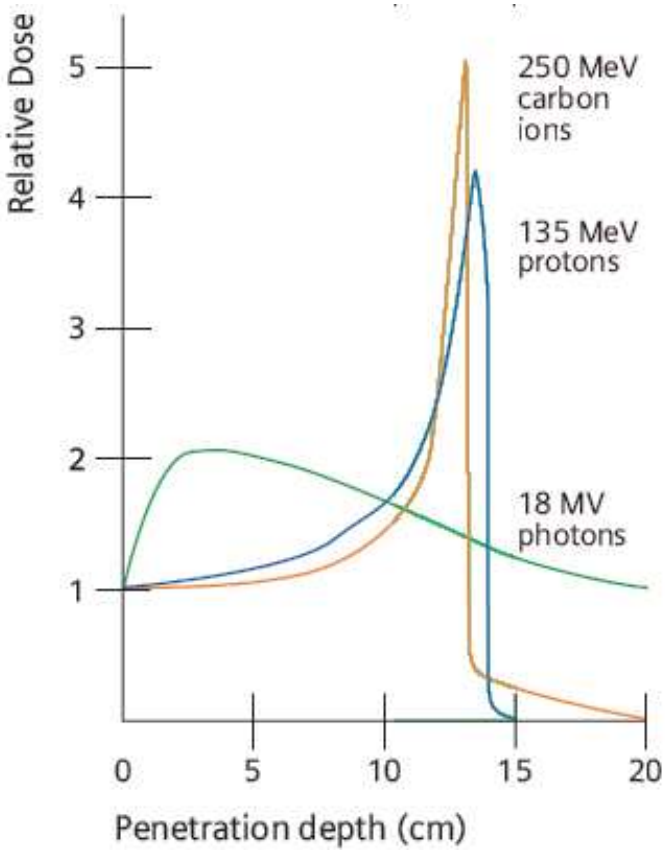

Figure 3.1: Comparison of the depth dose profiles of electromagnetic radiation with carbon ions and protons.

according to the Bethe-Bloch formula. This is caused by multiple scattering processes. In reality it yields an almost Gaussian energy loss distribution $f(\Delta E)$:

$$f(\Delta E) = \frac{1}{\sqrt{2\pi\sigma}} \exp \frac{(\Delta E - \langle \Delta E \rangle)^2}{2\sigma^2} \tag{3.3}$$

with

$$\sigma^2 = 4\pi Z_{eff}^2 Z N \Delta x \left(\frac{1 - \frac{\beta^2}{2}}{1 - \beta^2} \right) \tag{3.4}$$

The width of the Bragg curve depends on the penetration depth Δx of the particles and thus the Bragg curve is wider for particles with greater energy. In therapeutic praxis the active scanning is used to fill the target volume. If the Bragg peak is too sharp too many slices are needed, and thus it can be advantageous to widen the Bragg peak in order to decrease the overall treatment time. This is the case especially for tumors that are located close to the surface.

3.1 Lateral scattering

The lateral scattering of the therapeutic beam is at least as important as the depth dose profile. In order to limit the risk, the treatment is always planned to avoid the beam stopping in front of very sensitive regions. If the tumor is located close to such a region the beam will pass by to the side. Here the knowledge of lateral scattering is important when we decide how close the beam can get.

Lateral scattering mainly results from the Coulomb interaction of the projectile with the target nuclei. In addition the kinematics of the nuclear reactions contributes to the lateral width of a beam, predominantly at the distal side of the Bragg peak where the primary projectiles are stopped and the residual dose is made up with contributions of nuclear fragments only (Kraft, 2000). The angular distribution of the scattering is again gaussian:

$$f(\alpha) = \frac{1}{\sqrt{2\pi\sigma_\alpha}} \exp\left(-\frac{\alpha^2}{2\sigma_\alpha}\right) \tag{3.5}$$

with

$$\sigma_\alpha = \frac{14.1MeV}{\beta pc} Z_p \sqrt{\frac{d}{L_{rad}}\left(1 + \frac{1}{9}\log_{10}\frac{d}{L_{rad}}\right)} \tag{3.6}$$

where p is the momentum, L_{rad} the radiation length and d the thickness of the material.

During the first ACE measurements in 2003 it was found that the damage to samples placed outside the direct beam was minimal. Several approaches were used to test this and the details can be found in (Holzscheiter, 2005).

3.2 Conformal beam treatment

The increased dose and high biological efficiency at the end of the particle range can only be fully exploited with a so called target-conformal treatment. In very modern facilities for ion beam therapy such as PSI in Villingen and GSI in Darmstadt the dose is conformed to the tumour by lateral beam scanning. In this treatment technique, the target volume is divided into slices of equal particle range and each slice is treated by scanning the beam laterally over each slice. The slice to be treated is covered by a net of pixels that have to be filled by a definite but varying particle fluence according to the dose necessary to produce a homogeneous dose or biological effect.

Weber et al. (Weber et al., 2000) have recently proposed an alternative scanning method with a intensity-controlled longitudinal scan in the beam direction, called "depth scanning". This method yields the same conformity as a lateral scan system but requires a less expensive construction and control system. For depth scanning the target volume is divided into cylinders with the central axis parallel to the beam axis. Then the fast longitudinal scanning is applied in a series of such cylinders. It means that the Bragg maximum is continuously shifted along the central axis of the cylinder with a velocity up to $50\,\mathrm{cm}\cdot s^{-1}$.

In order to exploit the advantages of antiprotons in radiotherapy one of the described or a similar system should be applied in practise.

3.3 Annihilation

The antiproton nucleon annihilation occurs at rest or at low energies. The figures 3.2, 3.3 show $\bar{p}p$ and $\bar{p}n$ cross sections respectively. Annihilation is a process in which the baryons undergo a transition into mesons. The transition is viewed in the quark model basically as a rearrangement of all incoming quarks and antiquarks into quark-antiquark pairs. However the process in which some of the quarks and antiquarks annihilate and new quark-antiquark pairs are produced is also frequent. This makes the theoretical description particulary difficult.

During the annihilation event mostly pions are produced.

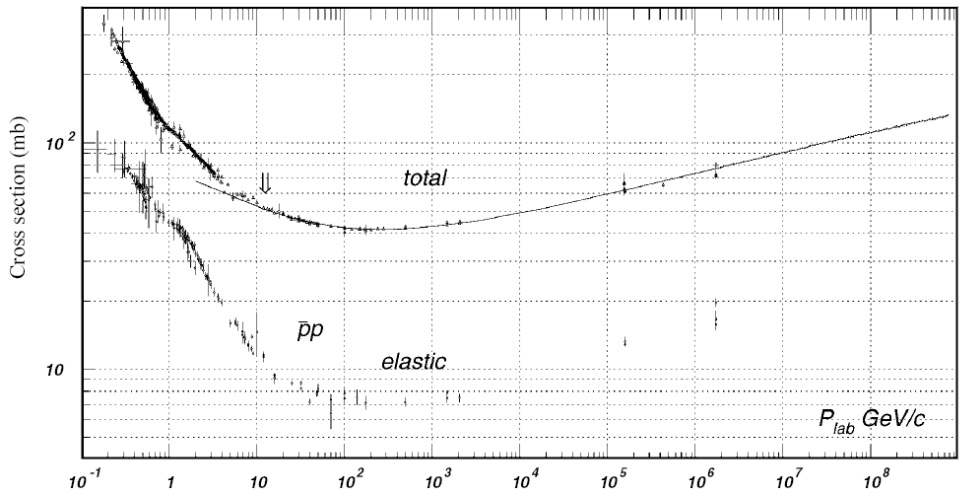

Figure 3.2: Total and elastic cross sections for $\bar{p}p$ collision as a function of laboratory beam momentum and total center-of-mass energy. Source (Eidelman et al., 2004).

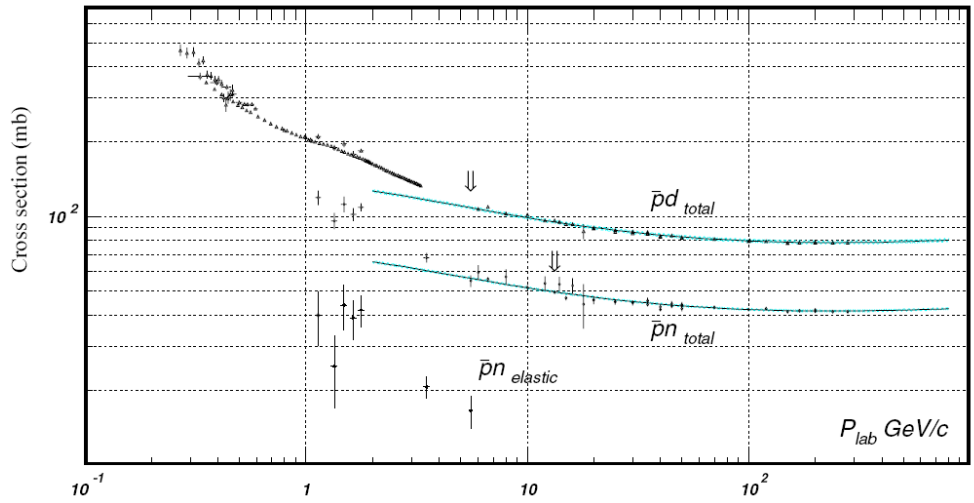

Figure 3.3: Total and elastic cross sections for $\bar{p}d$ (total only) and $\bar{p}n$ collisions as a function of laboratory beam momentum and total center-of-mass energy. Source (Eidelman et al., 2004).

The average pion multiplicity for the $\bar{p}p$ annihilation is estimated to:

$$n_\pi = 4.98 \pm 0.13, \;\; n_{\pi^\pm} = 3.05 \pm 0.04, \;\; n_{\pi^0} = 1.93 \pm 0.12 \tag{3.7}$$

The fraction of purely neutral annihilations (mainly from channels like $3\pi^0$, $5\pi^0$, $2\pi^0\eta$, and $4\pi^0\eta$ decaying to photons only) is (3.56±0.3)%. In addition to pions, η mesons are produced with a rate of about 7% and kaons with a rate of about 6% of all annihilations (Klempt et al., 2005), (Amsler, 1998).

The most detailed experiments to study the annihilation were performed at the LEAR facility at CERN, KEK facility in Japan and in Brookhaven National Laboratory. For review see e.g. (Amsler and Myhrer, 1991), (Amsler, 1998) and (Klempt et al., 2005). In most of the experiments antiprotons were stopped in liquid or gaseous H_2 or D_2 and thus the majority of the data can be found for hydrogen. The detailed survey of the annihilation mechanism is beyond the scope of this thesis and can be found elsewhere, e.g. (Klempt et al., 2005). I will give only a general review of the known facts and emphasize the details that are most important for the purposes of the imaging.

An antiproton stopping in hydrogen is captured to form an antiprotonic hydrogen atom. The highest probability of forming the $p\bar{p}$ system is for high principal quantum numbers: $n \sim 30$. The binding energy of the system corresponds to the binding energy of the electron ejected during the capture process. The deexcitation proceeds

via two different mechanisms. (a) Stark mixing, which dominates in liquid hydrogen and (b) the cascade to lower levels by x-ray or external Auger emission of electrons from neighboring molecules, which takes place mostly for the gaseous hydrogen.

In the liquid hydrogen collisions between the $p\bar{p}$ atom and neighboring molecules induce transitions from high angular momentum states, the process called Stark mixing. Thus the protonium annihilates with the angular momentum $\ell = 0$, from high S levels (S-wave annihilation). The initial states are spin singlets $^1S_0$ and spin triplets $^3S_1$.

In the gaseous medium the annihilation collision frequency is much lower and the annhilation occurs mainly with the angular momentum $\ell = 1$ (P-wave annihilation). Details of the S-wave and P-wave annihilations can be found e.g. in (Klempt et al., 2005). Annihilation from states with $\ell \geq 2$ can be ignored due to the negligible overlap of $\bar{p}$ and p in the atomic wavefunction. The branching ratio between the S-wave and P-wave annihilation depends on the density of the target. The dependance of the P-wave fraction on the density shows the figure 3.4.

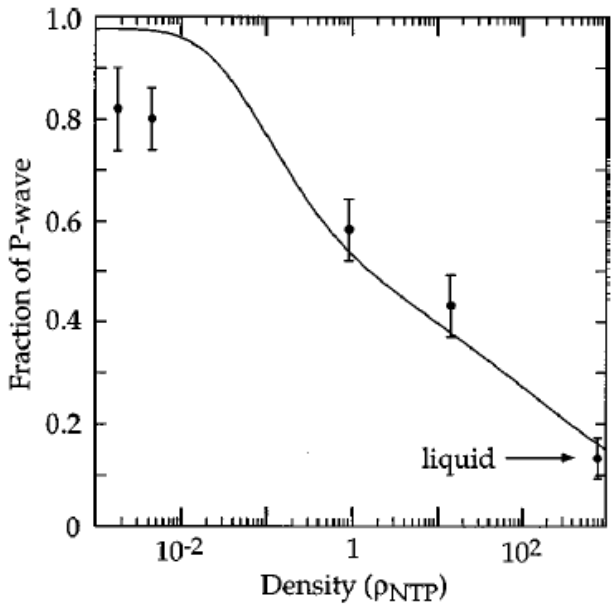

Figure 3.4: Fraction of P-wave annihilation as a function of hydrogen density (curve). The dots with error bars give the results from the optical model of Dover and Richard (1980) using two-body branching ratios. Source (Amsler, 1998).

The unified theory for the pion spectrum calculation was presented by Amado et al. in 1994 (Amado et al., 1994). In their picture the annihilation at rest is very rapid and results in a pion wave radiated from the annihilation vertex. The

pion wave is subsequently quantized using the method of coherent states (Horn and Silver, 1970). Applying the constraints of isospin and four-momentum conservation leads to the pion spectrum given in the Fig. 3.5. The results are in a very good agreement with experiments.

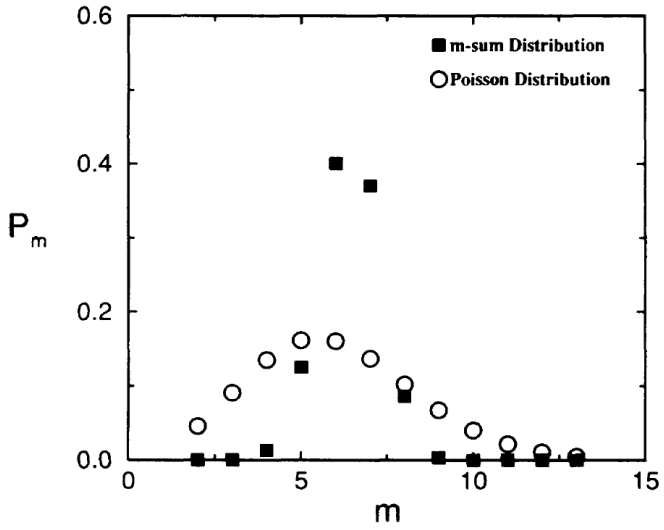

Figure 3.5: The probability, P_m, of having m pions in nucleon-antinucleon annihilation at rest as a function of m. The open circles refer to unconstrained coherent state and form a Poisson distribution. The solid squares include the constraint of four-momentum conservation and form the Gaussian distribution that agrees well with the experiment. Source (Amado et al., 1994).

3.4 Monte Carlo Simulation

For the simulation of the experiment we chose the Monte Carlo program GEANT4 (Agostinelli et al., 2003). GEANT4 is a toolkit for simulating the passage of particles through matter. It includes tools for designing the geometry of the system, the large set of materials and fundamental particles and most importantly, a wide range of physical processes. This enable us to generate a primary particle, to track its passage through the defined geometry and to record its interaction with the materials and the response of sensitive detectors.

In GEANT4 the mean energy loss of the antiprotons is calculated according to the restricted Bethe-Bloch formula:

$$\frac{dE}{dx} = KN_{el}\frac{Z_{eff}^2}{\beta^2}\left(\ln\frac{2\,m_e c^2\beta^2\gamma^2 T_{max}}{I^2} - \beta^2(1+\frac{T_c}{T_{max}}) - \frac{2\,C_e}{Z}\right) \qquad (3.8)$$

where N_{el} is the electron density of the medium, T_{max} the maximum energy transferable to the free electron, T_c the threshold energy above which the δ-rays are generated and C_e/Z is the shell correction term. The concrete values of the correction terms can be found in the GEANT4 documentation (Agostinelli et al., 2003). The accuracy of this formula is estimated as 1%.

The antiproton-nucleon reactions are implemented in GEANT4 with the quark level chiral invariant phase space (CHIPS) model. The antinucleon-nucleon annihilation algorithm is explained in detail (Degtyarenko et al., 2000). The first step of the CHIPS algorithm is the annihilation of antiprotons on peripheral nucleons, followed by the creation of an internuclear hadronic excitation (quasmons). The quasmon dissipates its energy and produces secondary nuclear fragments. The spectra of pions and nuclear fragments generated with the CHIPS model are in a very good agreement with the experimental data. The details of the CHIPS performance in antiproton-nuclear annihilation can be found in (Kossov, 2005).

In the simulation I use the $G4Q$CaptureAtRest process for all negative hadrons

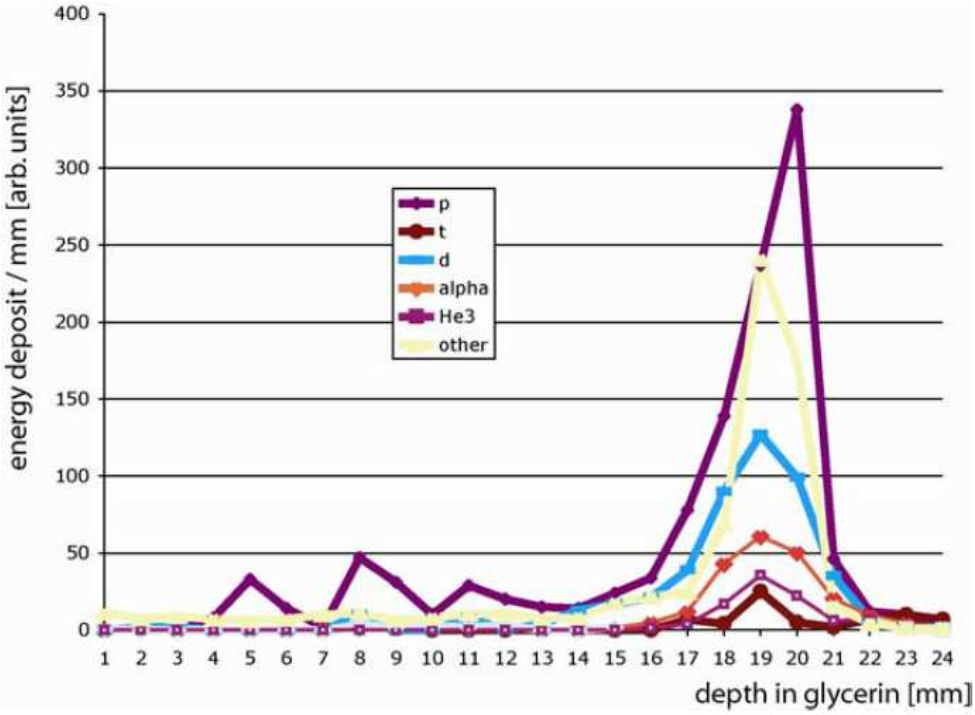

Figure 3.6: Energy deposition of an antiproton stopping in glycerin. The graph shows contributions of individual products of annihilation and inelastic collisions; namely of protons, deuterons, tritons, alpha particles, ^{3}He, and heavier fragments as a function of a penetration depth.

in GEANT4 Physics List. This applies the CHIPS algorithm for all capture at rest processes. Figure 3.6 shows the details for the energy deposition of antiprotons annihilating in glycerin. It shows the individual contributions of protons, deuterons, tritons, alpha particles, ^{3}He, and other (heavier) secondaries as a function of a penetration depth. A large fraction of annihilation products have a small momentum in the beam direction and thus are not emitted completely isotropically in space.

Figures 3.7 and 3.8 show the momentum spectra of particles emanating from the annihilation vertex in the GEANT4 simulation.

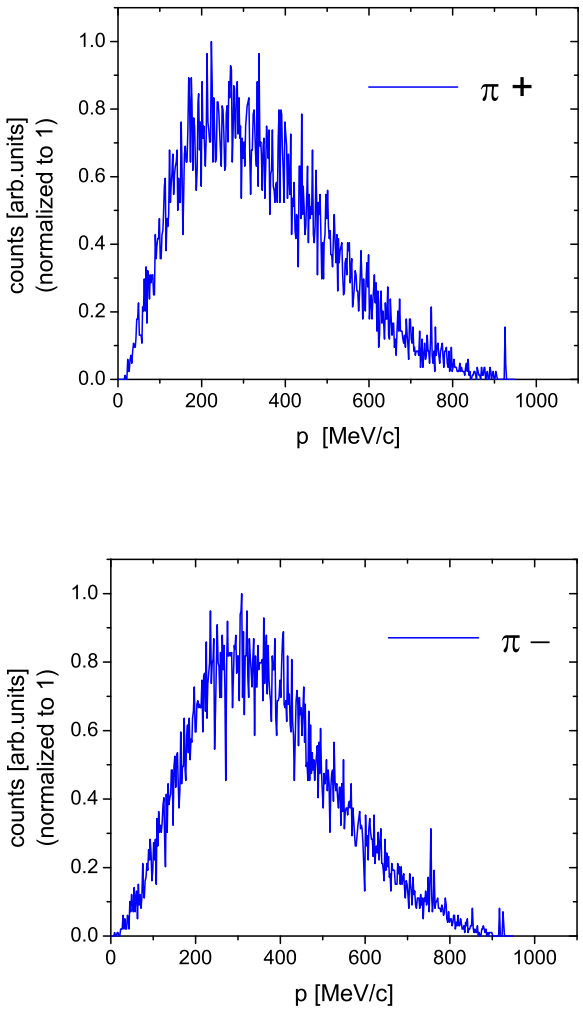

Figure 3.7: Momentum spectra of the particles created during simulated annihilation in Geant4. The upper panel shows spectrum of $\pi+$, the lower of $\pi-$.

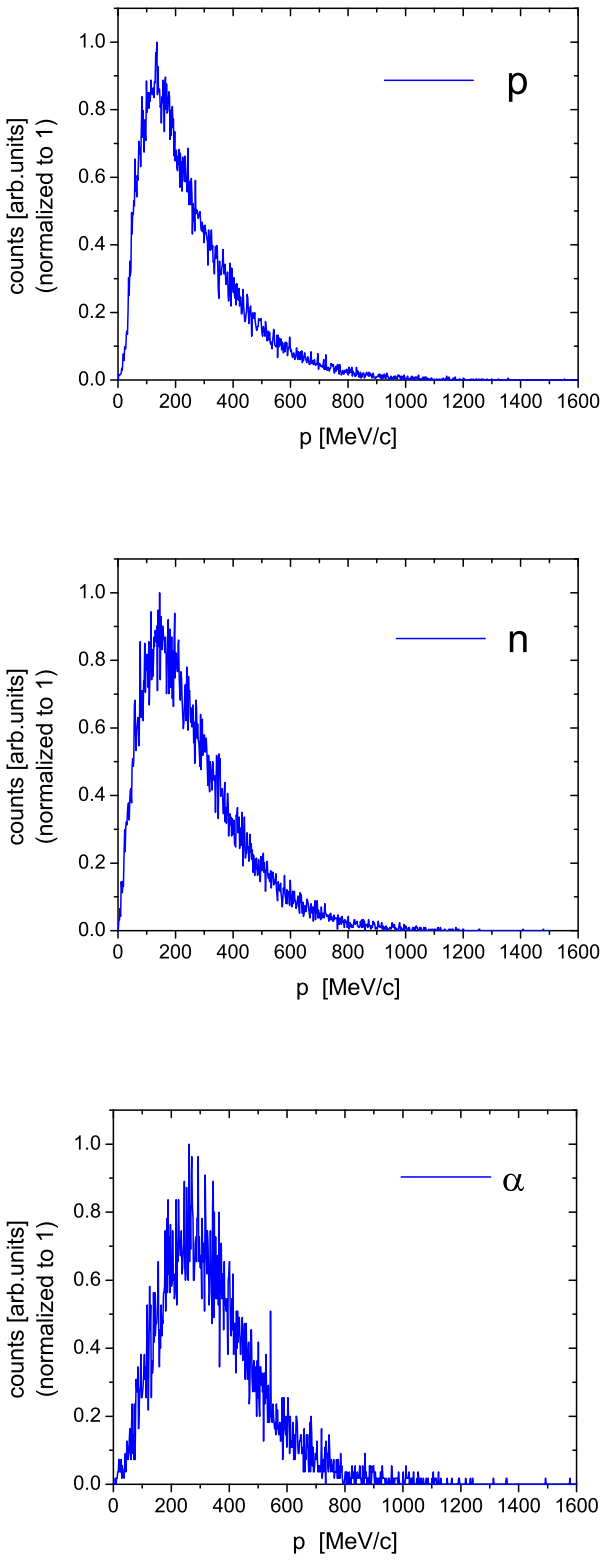

Figure 3.8: Momentum spectra of the particles created during simulated annihilation in Geant4. From the topmost panel: protons, neutrons and α particles.

Chapter 4

The Prototype Experiment and its Analysis

The experiment that for the first time directly tested whether the pions emanating from the annihilation vertex could be used in the real-time imaging was performed in November 2005 at CERN by Michael Doser and Petra Riedler. The beam of antiprotons was extracted from the Antiproton Decelerator (AD).

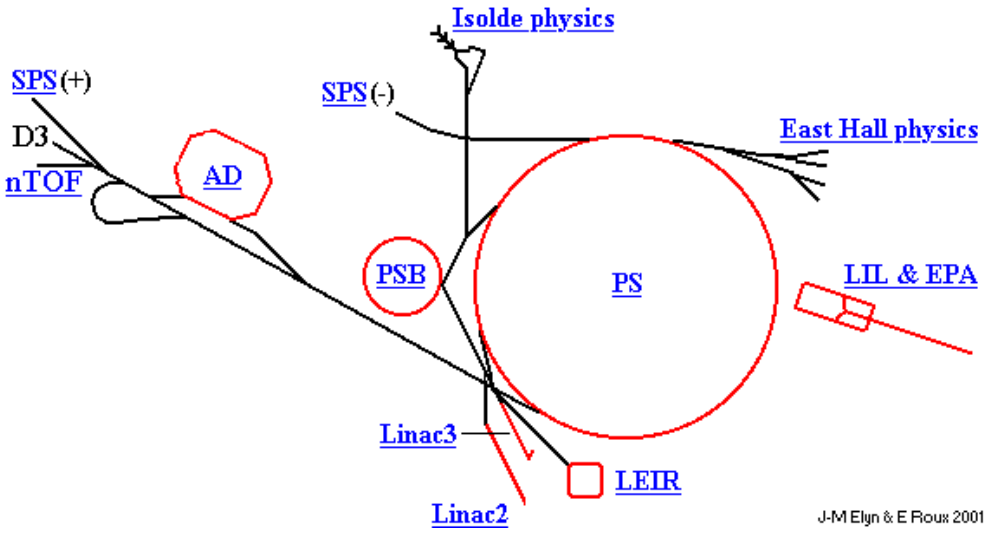

Figure 4.1: The scheme of PS experiments including the AD ring.

The AD is a facility which produces a low-energy beam of antiprotons. A proton beam at 26 GeV/c is extracted from PS (Proton Synchrotron) and delivered onto a Copper or Iridium target. Of 1.5×10^{13} protons about 5×10^{7} antiprotons at 3.57 GeV/c are created and then the beam is decelerated. The deceleration proceeds

in several consecutive steps (Fig. 4.2) and takes 100 s. At first stochastic cooling is applied and the beam is decelerated down to 2 GeV/c. Afterwards electron cooling slows the beam down to 100 MeV/c. At the end 3×10^7 antiprotons are available at low energy for the experiments. The detailed information about AD can be found in e.g. (Belochitskii et al., 2004).

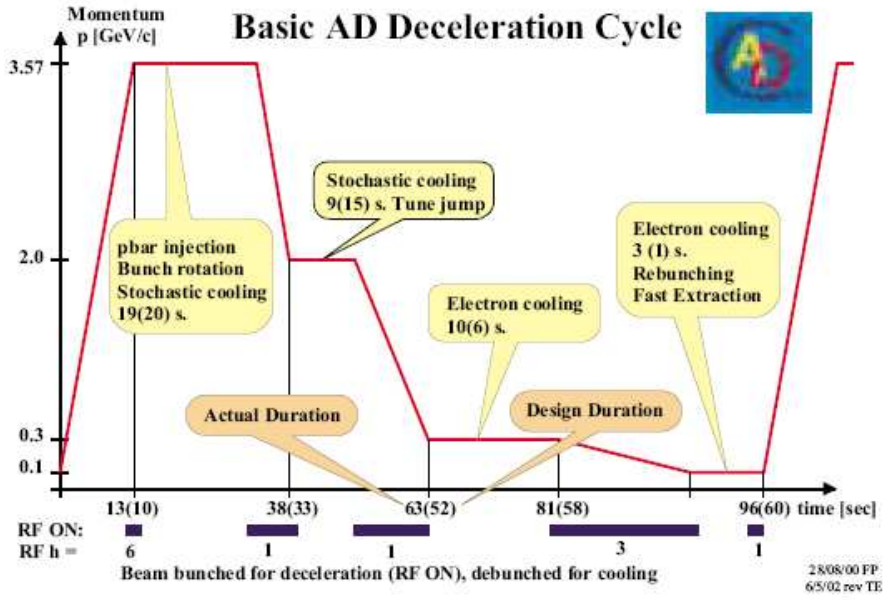

Figure 4.2: AD cycle.

For the ACE experiment a pulse of 3×10^7 antiprotons with $p = 300$ MeV was extracted from the AD was sent onto a water target (a cylinder of a radius 2.5 cm and length 20 cm). The antiprotons stopped simultaneously in the water. The stopping distribution is expected to have the form of a sigmoid, with a width of 3 cm transverse to the beam axis, and 2 mm along the beam axis. The charged pions were emitted isotropically and a fraction of them was detected. A scheme of the setup used is sketched in the Fig. 4.3.

A standard multiplane silicon pixel detector was chosen to detect charged pions. Particulary a prototype of the ALICE chip, developed at CERN was used. The ALICE1LHCB Pixel chip contains 8192 pixel cells, each with a size of $50 \times 425\,\mu\text{m}^2$. The cells are arranged in a matrix with 32 columns and 256 rows. The sensor thickness is 300 μm and the chip thickness 725 μm. Three such pixel chips were placed 193 cm far from the water target, aligned as is shown in the Fig. 4.3.

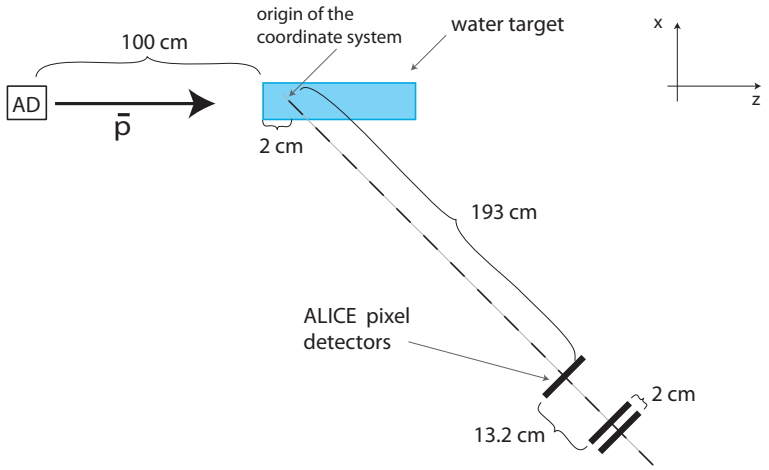

Figure 4.3: The experimental setup used in the first experiment to test the imaging potential, performed at the AD at CERN in November 2004. The figure shows the setup in a top view.

The aim of the experiment was to show that the tracks of detected pions can be reconstructed and the parameters of the stopping distribution gained. Unfortunately we cannot expect any correlation among the registered pions, because it is very unlikely that any given pair would come from the same annihilation vertex. This makes the reconstruction of the parameters particulary difficult.

I address the analysis of this experiment in the next section. I present there a GEANT simulation of the experiment and an algorithm developed for a reconstruction of the stopping distribution parameters. The algorithm is applied on experimental and simulated data. Limitations of the current setup are clear and therefore I propose an improved experimental setup for the next experiments. This proposal is described in the next chapter.

4.1 GEANT4 simulation

I have simulated the experiment using the Monte Carlo package GEANT4, shortly described in the section 3.4. For a schematic top view of the setup see Fig. 4.3. The origin of the coordinate system was located on the beam axis, 2 cm deep in the water target, as is shown in the figure. The y axis points out of the figure. The antiprotons with energy 300 ± 0.1 MeV came from the source located at $z = -1.02$ m, i.e. 1 m away from the water target. The distribution of the beam transverse to the beam axis was Gaussian with the width of 3 cm. The water target was surrounded by air under standard conditions. The set of the the three silicon pixel detectors was

rotated 45 degrees about the y axis, facing the volume where most of the annihilation events were expected to take place. For the detector location see the scheme.

In order to decrease the overall run time of the simulation I used detectors 100 times larger, i.e. 10×10 ALICE chips described above. Thus each of the detectors had 2560 rows and 320 columns. The width of the chips was $300\,\mu$m.

The detectors as well as the water target was set sensitive and the coordinate of each pixel receiving a hit was registered. The exact coordinate of the annihilation vertex was saved only when a product of this annihilation event hit the detectors.

A preview of a typical event generated with GEANT4 is in the Fig. 4.4.

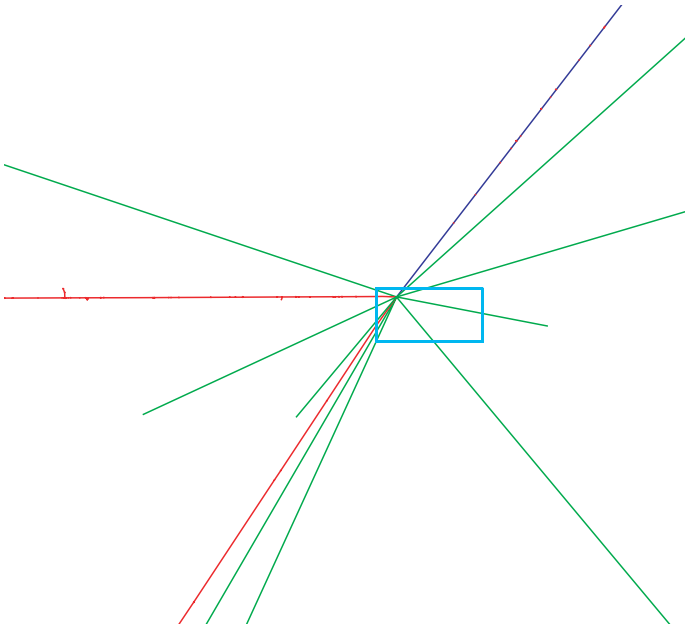

Figure 4.4: A top view on the GEANT4 simulation of an antiproton stopping in a water target. The red horizontal red line on the left side shows a $\bar{p}$ coming from the source, the turquoise rectangle is the water target. Colors of the lines correspond to the charge of the particle: red – negative, blue – positive and green neutral. The majority of the green lines are γ.

4.2 Algorithm for the experiment analysis

An algorithm for the reconstruction of the stopping distribution analysis has been developed. The reconstruction is not very precise with the experimental design described above but the ideas can be used in the improved experimental design that is suggested in the next chapter. Through the whole document the system of coordinates introduced in the figure 4.3 is used. The origin of the system is located

at the beam axis, 2 cm deep in the water and the y axis is pointing out of the figure. The beam axis is identified with z axis. The program is written in the C++ language and consists of the following parts:

1. Input file reading.
2. Particle tracking and searching for the z-peak.
3. Reconstruction of the stopping distribution parameters along the x axis.
4. Reconstruction of the stopping distribution parameters along the y axis.

As input the files generated with the Geant4 simulation were used. The files consist of the pixel coordinates, i.e. a row and column numbers. The original plan was to use the data measured with the experiment. Unfortunately during the data taking technical problems occurred and the data were not collected properly. However as it is shown later, with this experiment design the reconstruction would not be possible.

In the first part the program reads the coordinates of the pixels that received a hit. No complicated cluster finding algorithm is included because for the experiment analysis it will be more convenient to use a program for precise hit localization developed by the ALICE group specifically for the ALICE chips. While reading the output of a Geant4 simulation only hits that are not wider than 2 pixels in each direction are validated. Also, only the tracks that intersect all three detector planes are taken into account. The first detector (the one closest to the target) optimal occupancy, for good analysis is 25 - 35 hits/cm^2. With less hits the program finds the z-peak location ($\pm$ 1.5 mm) and the y distribution fairly well. However it is impossible to describe the x distribution. With higher occupancy the number of fake tracks is too high to trust the algorithm output. The top limit for the algorithm is the occupancy of 50 hits/cm^2. With little adjustment the algorithm can work with an occupancy of 3 hits/cm^2.

The second step is the particle tracking. I use the knowledge of the geometry of the experimental layout and search only for the tracks that come from the target direction. The reading starts from the third plane (the most distant one) and the hits from the other two detectors are added to form a track only if the track points in the target direction. In order to reduce the number of fake tracks I only search for tracks coming from a part of the water cylinder, which is chosen to include the area where the Bragg peak is expected to be located plus a sufficiently large area that

surrounds it. For example, when I searched for the Bragg peak which was expected to be 2 cm deep in the target I assumed that it would be not deeper than 4 cm.

I perform different tracking for the analysis in each direction. While searching the z-peak, the sharp peak in the depth dose profile I make the following assumption: only a negligible fraction of annihilations occur deeper than 4 cm and the stopping distribution does not depend on y. I search the tracks coming from a narrow slice $x \in (-25, 25)$ mm, $y \in (-2, 2)$ mm.

If the occupancy of the detectors is not too high (see above) I find approximately the right number of tracks. It is very unlikely that any pair of tracks come from the same annihilation vertex. An intersection of each of the tracks with the target volume is a line segment, up to few centimeters long. There is no way how to determine where exactly on this segment the annihilation occurred.

To determine the location of the z-peak I use the fact that the distribution transverse to the beam axis is regular. It means that there is approximately the same number of particles coming from the x > 0 half of the water target as from the x < 0 half. Thus the central line of the bunch of the reconstructed tracks intersects the central beam line (z axis) at the point where the z-peak is located. The central line is found so that intersections of all the tracks with two arbitrary planes, parallel to the detectors are found. In each of these planes a central point is calculated according to:

$$\vec{R} = \frac{\sum_{i=1}^{n} \vec{r_i}}{n} \tag{4.1}$$

where $\vec{r_i}$ correspond to the intersections and n is the number of tracks. The central line is obtained with connecting these two points.

The main problem for the precise reconstruction is the finite width of the pixel (0.425 mm), which hinders accurate track reconstruction. The error on the z axis for a single track can be in the worst case 15 mm. However, if the statistics is high enough these errors cancel and the error for the central line is reduced to 2 mm.

The reconstruction along the y axis gives the best results, because of two reasons: 1) the detector resolution in the vertical direction is 8.5 times better than in the horizontal, 2) the detectors are not rotated about the z axis and thus the reconstructed tracks include the plane y = 0 only at a small angle. Hence the error in estimate of the y coordinate of the annihilation is much smaller. To reconstruct the distribution I use a method which I later on refer to as a scanning method. I calculate how many

occupancy (hits/cm^2)	depth of z-peak (mm)	σ_y (mm)
3	18.4	23.5 ± 7.4
6	17.4	24.8 ± 6.7
17	17.3	27.2 ± 6.3
25	18.3	18.3 ± 1.9
30	18.9	17.8 ± 1.7
35	18.8	19.6 ± 1.8
50	19.3	19.1 ± 2.4

Table 4.1: Reconstruction of the simulated experiment. The occupancy is given for the the 1$^{\text{st}}$ detector plane (the plane which is closest to the target), σ_y is a half width of a gaussian fit to the found distribution. The real parameters were: depth of z-peak = 18.4 mm, $\sigma_y = 17$ mm.

tracks come from the slices $y \in (y_c, y_c + 2)$ mm and $y \in \{-25, -23, .., 23\}$ mm, i.e. the program scans the target volume along the y axis and counts the number of tracks in each of the scanned part. The results obtained are plotted and compared to the simulation output in the Figure 4.6.

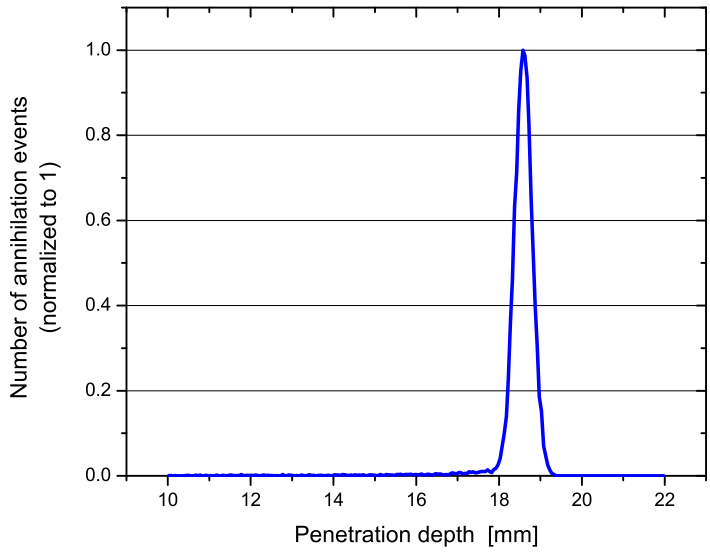

Figure 4.5: Stopping distribution of antiprotons in water as a function of penetration depth, simulated with Geant4.

In Table 4.1 the results found with the algorithm for the samples of different occupancies are summarized and σ_y comes from a gaussian fit. In the Geant4 simulation the stopping distribution was a sigmoid with a width of 34 mm transverse to the beam axis and 3 mm along the beam axis. The z-peak was located at the depth of 18.6 mm. The profile of the peak calculated with Geant4 is shown in the Fig. 4.5.

The tracking for the x axis analysis is performed for a volume of $x \in (-25, 25)$ mm, $y \in (-2, 2)$ mm and $z \in$ (z-peak $-$ 10, z-peak + 10) mm. Intersections of the tracks found with a plane z = z-peak are found. The projection of the intersections to the x axis yields the distribution in the x direction. The results obtained are plotted and compared to the simulation output in the Figure 4.6.

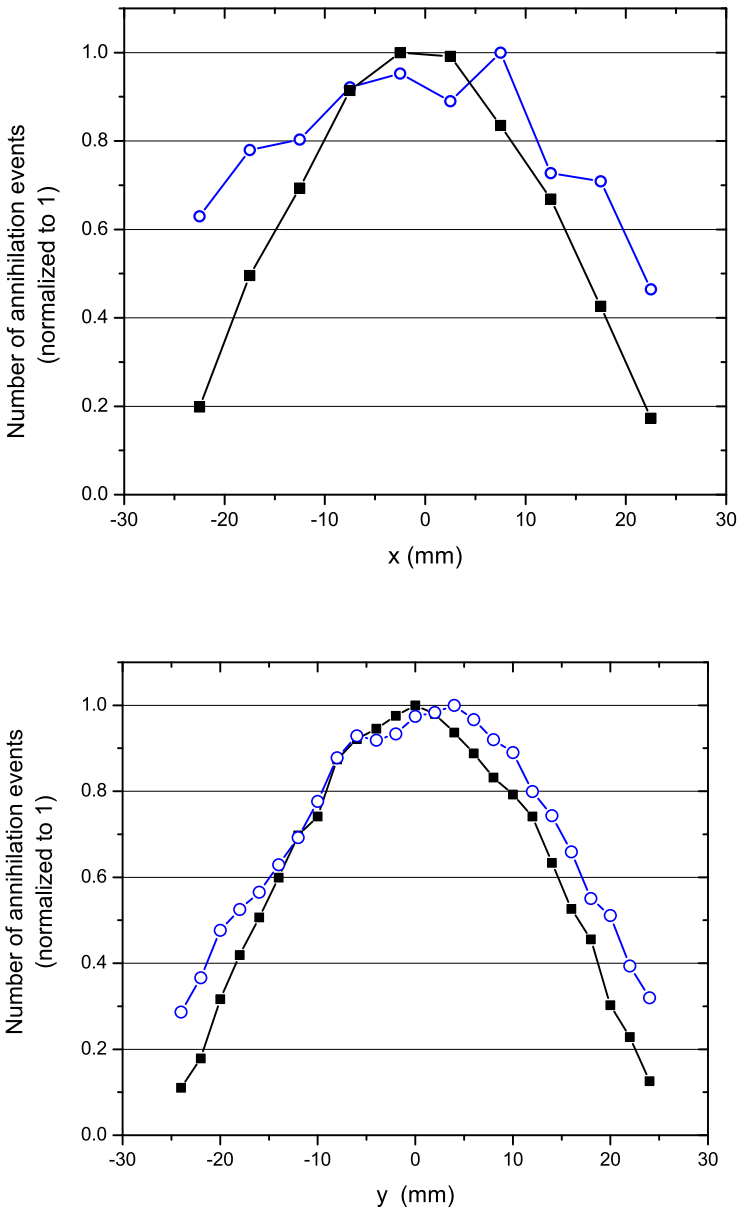

Figure 4.6: Stopping distribution of antiprotons in water along the x (upper panel) and y (lower panel) axis. The black squares show the output of Geant4 simulation, blue open circles the reconstruction performed with the algorithm described above. The occupancy of the 1st detector was 30 hits/cm^2.

4.3 Conclusion

Apparently the reconstruction is not very accurate. The distribution in the x direction is not reconstructed precisely. In the z direction it is only possible to determine an approximative position of the peak. The reconstruction precision is probably sufficient for therapeutic purposes.

I do not think that there is a way to significantly improve the algorithm. The reasons for the inaccuracy lie in the design of the experiment. As was mentioned before, even when the right track is reconstructed it is not possible to determine where exactly on the intersection of the track with the target the annihilation occurred. Putting some assumptions on the symmetry of the layout it is possible to estimate where the z-peak was located but i didn't find a way to reasonably estimate the width of the peak.

Making the intersection of all the tracks with the plane z = z-peak, i.e. with the plane where the majority of annihilations occurred a rough estimate of the x axis distribution can be made. However it is not possible to select the tracks that belong to the annihilation events which took place in this plane and the distribution is blurred. The best estimate I got is shown in the Figure 4.6.

The other problem is, that the analysis was performed on 100 times larger detectors. The original experiment was carried out with detectors of surface equal $174.08\,\mathrm{mm}^2$ and when I assume that the annihilation products were emitted as they are emitted in Geant4 it received about 330 hits. With the occupancy of $190\,\mathrm{hits/cm}^2$ the algorithm would not work anyway.

Significantly improved results can be obtained with rather small changes in the experimental setup. Such changes are described in the next chapter.

Chapter 5

Proposal For The Next Experiment

A clear conclusion of the last chapter is that a single set of detectors is not sufficient for a good three dimensional reconstruction of the stopping distribution. Another important observation is that the scanning method (the method used in the previous chapter for the reconstruction along the y axis) proved to be successful for the detector situated parallel to the axis of interest (in that case the y axis).

The aim was to improve the reconstruction with as few added detectors as possible. I propose two different layouts and describe their advantages and disadvantages. The simulations were written again in GEANT4, the program for the reconstruction is described in detail in the Appendix.

In simulations a different target was used than in the original experiment. Here I used a cube of water with an edge length of 10 cm. The reasons for the change was to approximate a prospective medical target, in this case the head. This approximation is important because the pixel detectors detect all charged particles, not only the pions coming directly from the annihilation vertex. The annihilation products, after emanating from the annihilation vertex collide further. Products of these collisions also reach the detectors and blur the distribution of pions. The number of these particles depend on the distance that the annihilation products travel in the water, namely on the size of the target. The table 5.1 shows the number of hits generated by various particles in the detectors situated behind and parallel to the target. Two different target sizes are presented: a cube with edge length equal to 10 cm and 20 cm.

The most problematic particles are e^- and e^+ which are either delta electrons or stem from pair production. In both cases they do not come from the annihilation

particle	Hits [%] target edge = 10 cm		Hits [%] target edge = 20 cm	
	Parallel	Perpendicular	Parallel	Perpendicular
π^-	19.4	29	16.7	24.8
π^+	16.6	19.6	14.7	15.6
e^-	31.5	24.9	38.4	35.1
e^+	9.2	9.7	14.9	15.1
p	14.1	12.5	8.8	6.3
d	1.7	0.8	0.5	0.1
μ^-	4.2	1.8	3.3	1.6
μ^+	3.2	1.7	2.6	0.9

Table 5.1: The percentage of hits generated by various particles in the detector parallel and perpendicular to the beam axis. As a target was used in both cases a cube of water. The first column shows the results for the cube of the edge length equal 10 cm, the second column of the edge length equal 20 cm. The width of the beam at FWHM was 3 cm.

vertex, which makes them particulary problematic. On the other hand they mostly do not have very high energies and thus scatter easily. The hits that they leave in detectors often do not cross the detectors on a straight trajectory and therefore are not included in the bunch of reconstructed tracks. Although there are less of them in the perpendicular detector, they have higher energies, which makes the reconstruction from these detectors less precise.

There are also a significant amount of protons hitting the detectors. They are emitted during the nucleus fragmentation following the annihilation process. A spectrum of these protons is given in figure 3.8. The protons mostly come from the annihilation vertex, but often do not have sufficient energy to leave a straight track in the detectors. From the table 5.1 it follows that if the passage from the annihilation vertex through the target is longer far less protons reach the detectors. The number of registered electrons slightly increases with the target size.

5.1 A layout using two detector sets

The first proposed design consists of two sets of detectors instead of one. One of them is designated to recognize the depth dose profile and the other one to reconstruct

the distribution transverse to the beam axis. A schematic view of the design is shown in the figure 5.5. The occupancy optimal for both sets of detectors was found to be $15-40\,\mathrm{hits/cm^2}$, the maxi occupancy for a valid output is $60\,\mathrm{hits/cm^2}$. The results are always presented for two different occupancies: 20 and $40\,\mathrm{hits/cm^2}$. The detectors located parallel to the beam axis serve for reconstruction in the z direction. Therefore the detectors were rotated $90\,^\circ$ about the x axis in order to achieve better resolution in the z direction.

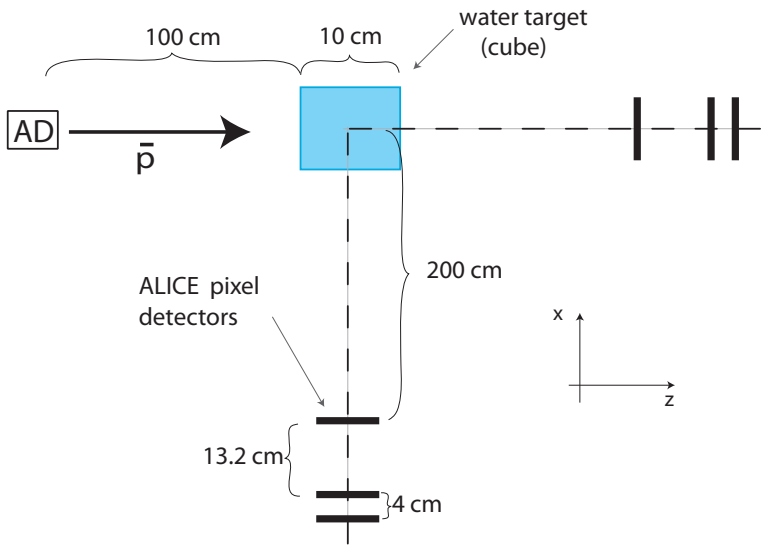

Figure 5.1: A scheme of first proposed experimental design. Top view.

The reconstruction program uses the method of the central line for a precise localization of the z-peak. This method is described in the previous chapter where it was also used for the localization of the annihilation peak. With this setup the peak is localized with a significantly improved precision ($\pm\,0.7\,\mathrm{mm}$), compared to $\pm\,2\,\mathrm{mm}$ in the previous chapter. The width of the peak is estimated with the scanning method. The wider the peak is the better this method works. For 5 mm and more is gives fairly well estimate. However for the very narrow peaks the estimate is quite unprecise, as you can see in the figure 5.2. The main reasons are the impossibility to localize the annihilation event on the intersection of the track with the target volume and the particles that are not emitted from the annihilation vertex. These are mostly e^- and e^+, whose origin is described above. They comprise one third of all the hits and thus blur the distribution significantly. The figure 5.2, (a) shows the output of the reconstruction compared to the simulated data. Using the central line method in this example the peak was determined to be at the depth = 18.8 mm

when the occupancy was 20 hits/cm^2 and 18.1 mm when 40 hits/cm^2. Geant4 output peak was at 18.5 mm.

It should be kept in mind that in medical applications the Bragg peak will be perhaps enlarged in order to reduce the overall treatment time. In the lateral scanning method, described in the section 3.2 a typical width of the slice is 4-5 mm, which corresponds to the width (FWHM) of the Bragg peak. In the depth scanning method the width of the Bragg peak corresponds to the width of the tumor (up to few cm). It is therefore necessary that the imaging method recognizes the wider peaks well. I made simulations with 2 different spread-out Bragg peaks, one with a width of 5 mm and the second one with a width of approximately 1 cm. Results of the reconstruction for these peaks are shown in figure 5.3.

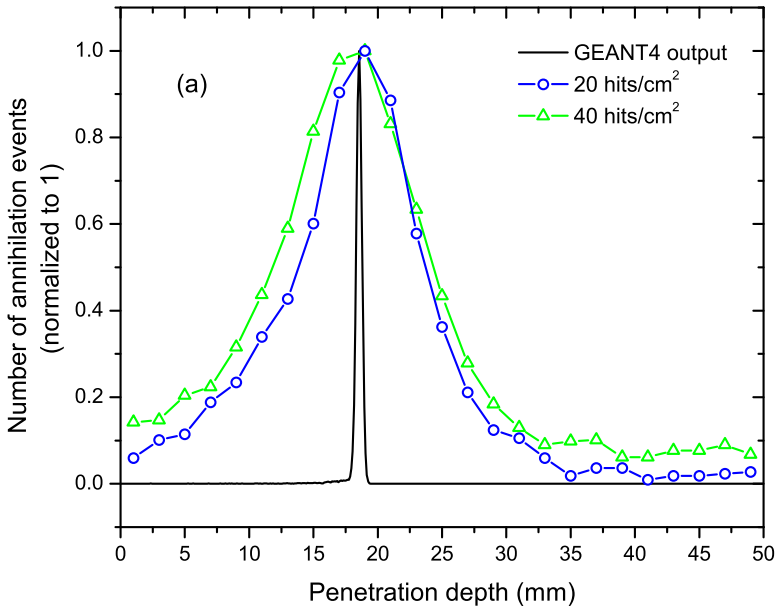

Figure 5.2: Stopping distribution of monoenergetic antiprotons in a water target along the beam axis. The black lines show output of Geant4 simulation, the result of the reconstruction is shown for the occupancy of 20 hits/cm^2 (blue open circles) and 40 hits/cm^2 (green triangles).

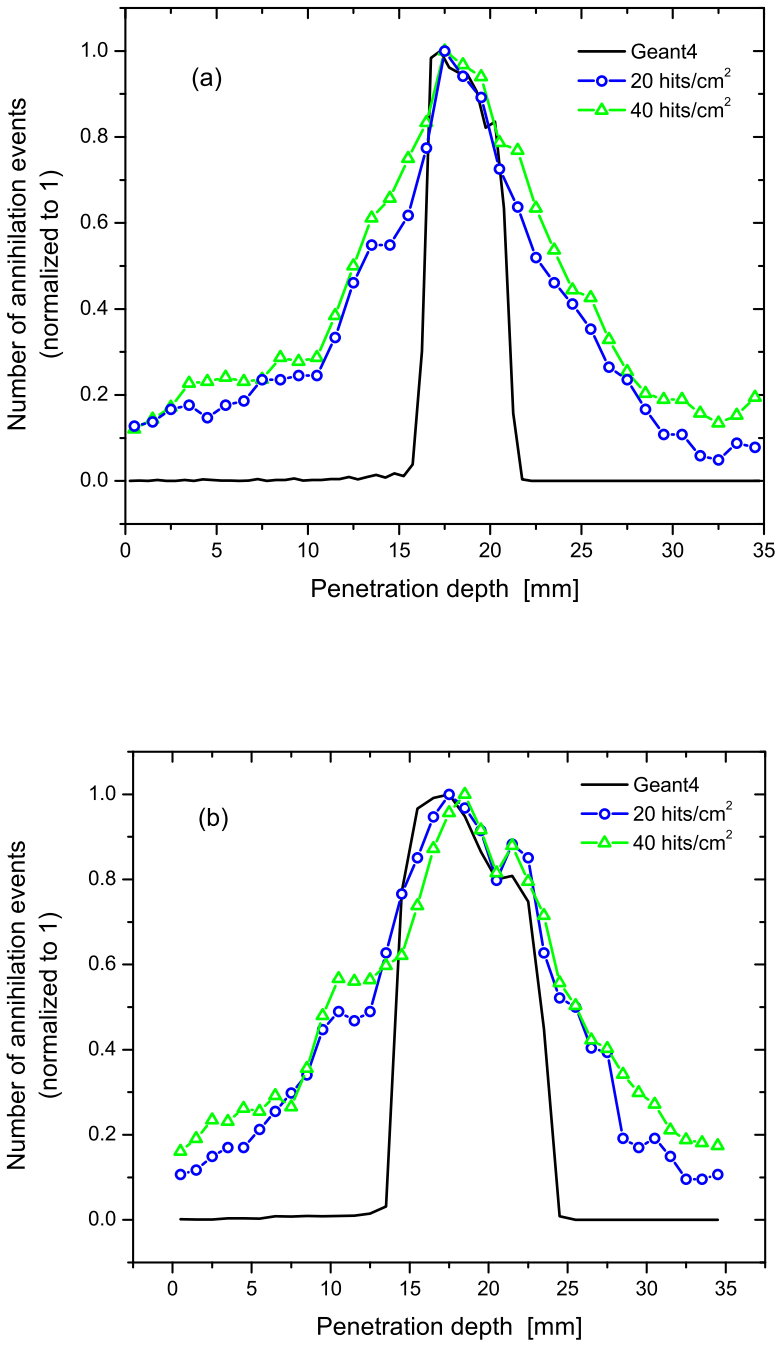

Figure 5.3: Stopping distribution of antiprotons in a water target along the beam axis for two different spread-out Bragg peaks. The black lines show output of Geant4 simulation, the result of the reconstruction is shown for the occupancy of 20 hits/cm^2 (blue open circles) and 40 hits/cm^2 (green triangles).

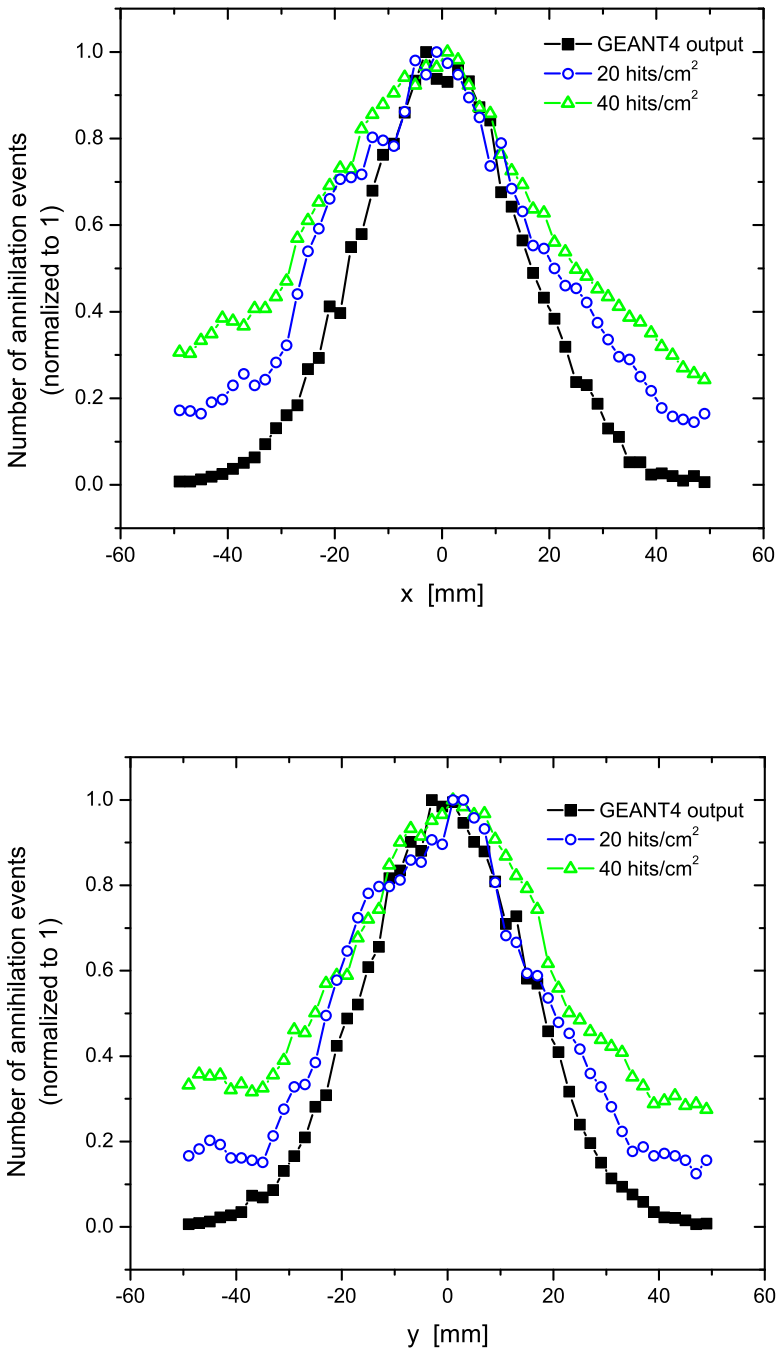

Figure 5.4: Stopping distribution of antiprotons in a water target, transverse to the beam. The black lines show output of Geant4 simulation, blue open circles and green triangles the reconstruction gained with the detector perpendicular to the beam line. The occupancy was 20 hits/cm^2 for the blue open circles and 40 hits/cm^2 for the green triangles.

The detector set perpendicular to the beam axis, placed behind the target serves for the reconstruction of the parameters describing the shape of the annihilation volume transverse to the beam axis. In order to get a fairly good resolution in both directions (x and y) the middle detector is rotated 90 °. To accommodate differing needs, detectors can be rotated in a different way or additional planes added. For the reconstruction the scanning method was used again. Figures 5.2 and 5.4 show results of the reconstruction.

The perpendicular detectors receive approximately three times more hits than the detector placed parallel to the beam, if they are both the same distance from the annihilation sigmoid. It can be advantageous for low intensity beams, but can cause problems if the intensity is high.

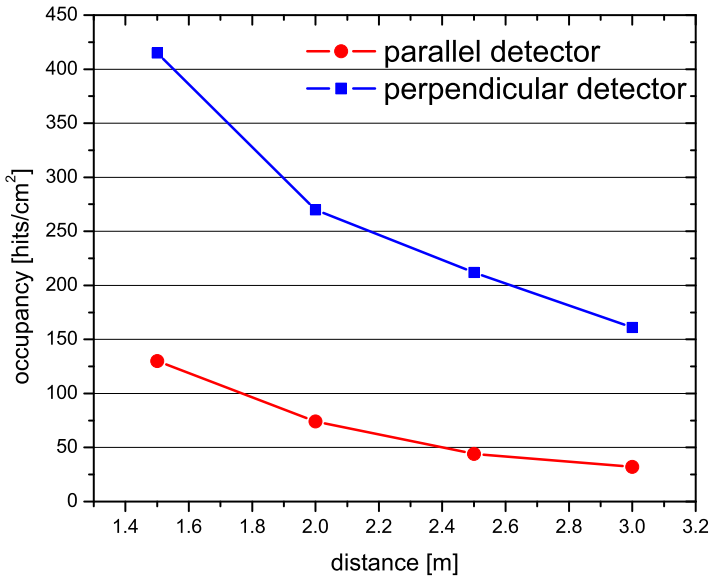

Figure 5.5: Occupancy of a parallel and a perpendicular detector after a pulse of 10^7 antiprotons plotted versus a distance of the detectors from the target. The target was a cube $10 \times 10 \times 10$ cm. Red circles show the occupancy of the parallel detector, blue squares the occupancy of the perpendicular detector.

5.2 A layout using three detector sets

The problem with the previous setup is that the detector set located behind the target receives too many hits compared to the second detector. Therefore for the

high intensity beam a setup with detectors located only parallel to the beam line would be more convenient. The setup I propose uses three sets, each for a reconstruction in one direction (Fig. 5.6). The detectors are always turned so that the highest resolution is achieved in the particular direction.

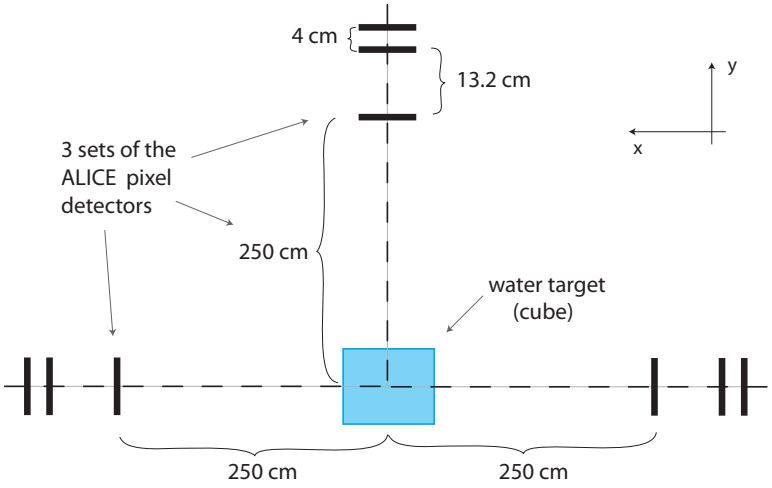

Figure 5.6: A scheme of the proposed experimental design. Beam view.

The reconstruction program again uses the central line method to find the precise location of the z peak and the scanning method to determine the width of the peak. The results for the range reconstruction are presented in the previous section (5.1). The results for the transverse beam profile are presented in figures 5.7 and 5.8, always for detector occupancies of 20 and 40 hits/cm^2. The figures show results for two different beam profiles, one with beam width 0.5mm and other 1 cm at the FWHM. For very narrow peaks (only few mm at the FWHM) the accuracy of the reconstruction decreases as was explained in the previous chapter.

I tested how much the reconstruction would improve with better resolution of detectors. I used detectors of the same size, only the pixel size was 0.2125×0.02 mm instead of previously used 0.425×0.05 mm. The improvement is apparent for the range profile reconstruction, whereas for the transverse profile of the beam the difference can be hardly spotted. The reconstructions of the range profile for the better resolution is shown in the figure 5.9.

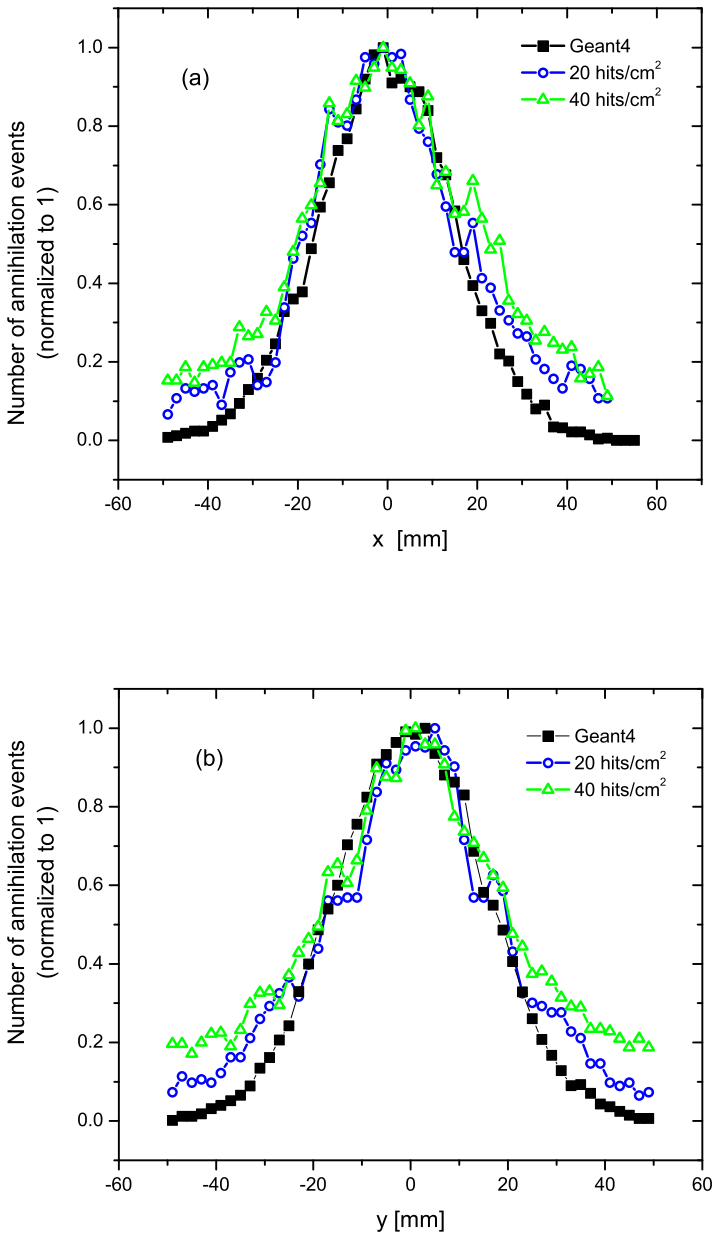

Figure 5.7: Transverse beam profile reconstructed with the 3 detector setup. Geant4 output (black squares) is compared with the reconstructed distribution for the occupancy of 20 (blue open circles) and 40 (green triangles) hits/cm^2. (a) Reconstruction in the x and (b) y direction.

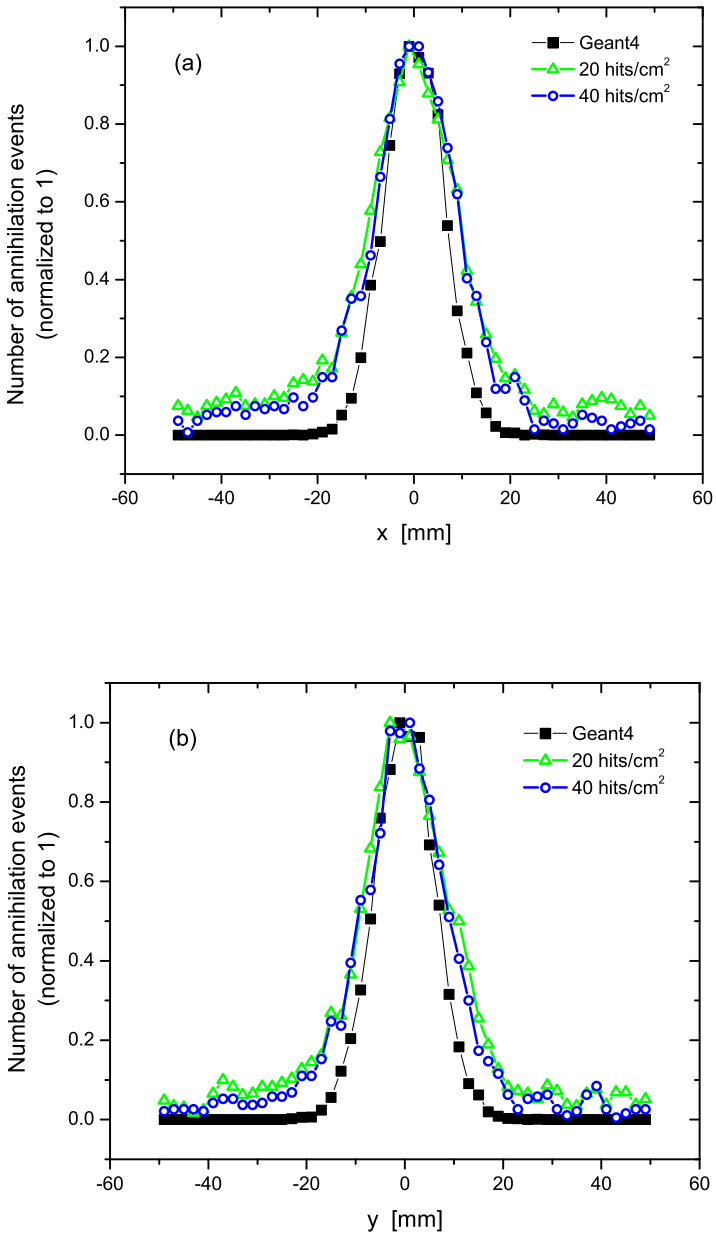

Figure 5.8: Transverse beam profile reconstructed with the 3 detector setup. Geant4 output (black squares) is compared with the reconstructed distribution for the occupancy of 20 (blue open circles) and 40 (green triangles) hits/cm^2. (a) Reconstruction in the x and (b) y direction.

An alternative to three detector sets is an arrangement of two detector sets where one of them reads in two directions. Apparently some precision is partly lost but it can be advantageous when the room for the experiment is not large enough. A reconstruction of a simulated experiment with two detector sets parallel to the beam line is shown in figure 5.10. The middle detector from the set that serves for the range profile reconstruction was rotated 90°, the second detector set was left as before. The target used in the simulation was a water cube with the edge length of 5 cm. The reconstructed curve is apparently much smoother than for the large cube, due to decreased scattering of the secondary particles. The central line method also worked well. The peak was determined to be at the depth = 18.8 mm for the alternative setup and 18.5 mm for the 3 detector setup. Geant4 outputs peak was at 18.5 mm. An additional improvement could be reached if another plane is added to the set reading in two directions.

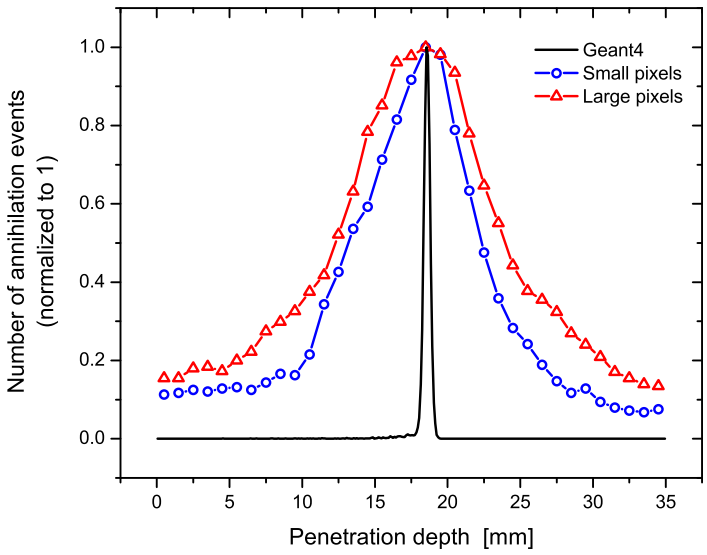

Figure 5.9: Reconstruction of the range profile using detectors with pixel size $0.2125 \times 0.02\,\text{mm}$ (blue open circles) and $0.425 \times 0.05\,\text{mm}$ (red triangles). Occupancy = $20\,\text{hits/cm}^2$.

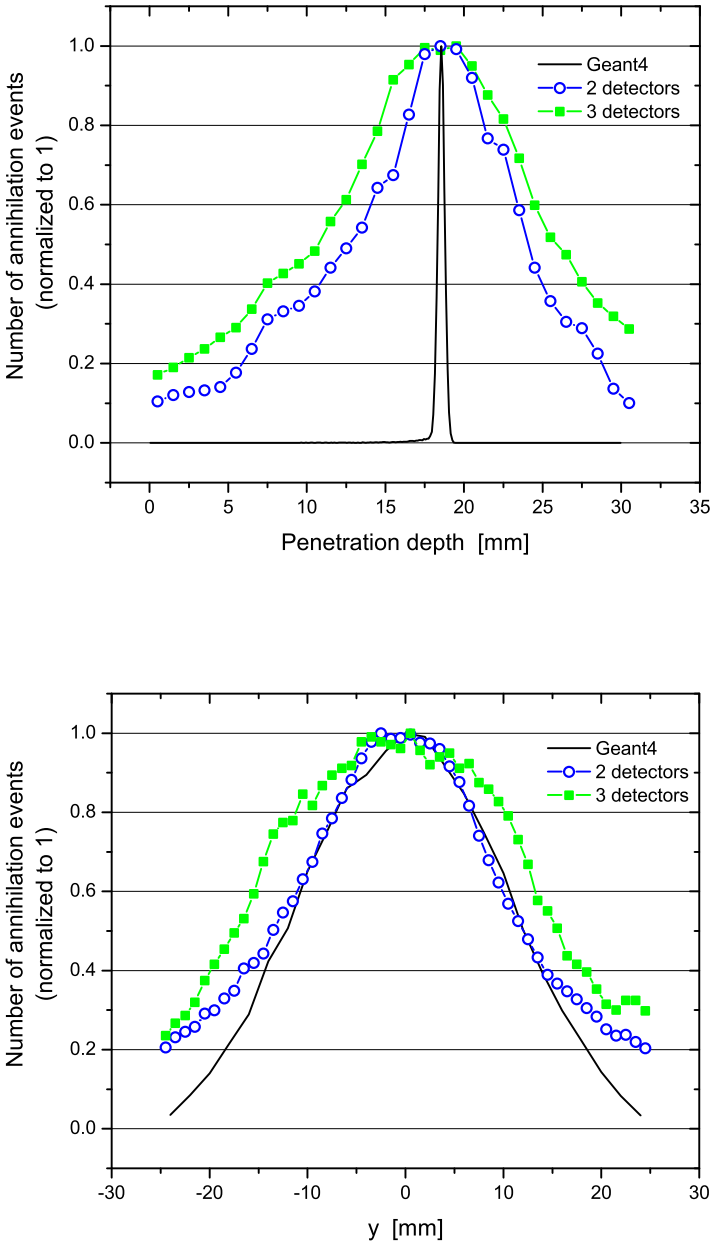

Figure 5.10: Comparison of the alternative setup with the middle detector plane rotated and the classical 3 detector setup. Reconstruction along (a) the beam axis and (b) the y axis. The detectors were located in the 2 m distance from the beam axis and the occupancy was 20 hits/cm^2. Black lines show the output of the Geant4 simulation, green squares the reconstruction from the alternative setup and blue open circles from the classical setup.

Chapter 6

Conclusions and further perspectives

In the present thesis I deal with the application of antiprotons for radiotherapy. The work is concentrated on the possibility of imaging the antiproton stopping distribution in the tissue.

At first the history of radiotherapy is revised and the motivation for the development of new, more efficient methods described. A part of the chapter is addressed to the physical principles of beam therapy and some theoretical background for antiproton annihilation.

An experiment to test if the particles emitted from the annihilation vertex of a biological phantom can be used for imaging and this was performed last year at CERN. An analysis of the experiment is presented in this thesis (chapter 4). Unfortunately the detectors did not work well during the data taking and virtually no data were collected. Therefore I could analyze only data acquired from a simulation. However, it was sufficient to show that the experiment design was not optimal and that the reconstruction would not have been possible even if the detectors had worked.

Observations of the experiment indicated what changes need to be made to the experimental design to improve the sensitivity to the stopping distribution parameters. Two designs were proposed and its performance simulated. The results are presented in the chapter 5.

Clearly the reconstruction of the stopping distribution is much more precise with the proposed experimental designs than it was in the original experiment. Of the two proposed designs the one using three detector set gives better results. However the design which uses only two detector sets can be advantageous for the low intensity

beams.

Another advantage of detectors placed parallel to the beam axis is that they can be rotated about the beam axis and preserve the same functionality. Therefore the arrangement can accommodate the room requirements. Apparently the reconstruction is more precise if the passage of particles through the dense medium (water or a body) is shorter. The rotation symmetry can be also used to arrange the detectors in such a way that the particle track is shielded as little as possible.

An important observation of the study is that it is desirable to decrease the intensity of the beam ejected by AD in order to get lower occupancies from the detectors. The other way is to place the detectors further away from the target. This can be however complicated because of the room available and can lead to a decreased accuracy of reconstruction if the detectors are too far away. Furthermore, it is desirable to scale up the surface of detector planes. The smaller they are the less precise the reconstruction.

The number of antiprotons used in a treatment session will possibly be lower than 3×10^7. For proton therapy it is usual to deliver the total dose of $50 - 70\,\mathrm{Gy}$ given typically in $4 - 6$ daily doses. Even if we assume that antiprotons would be four times more efficient maximally $70\,\mathrm{Gy}$ would be delivered at once. In the figure the dose delivered with one antiproton is depicted. From a simple

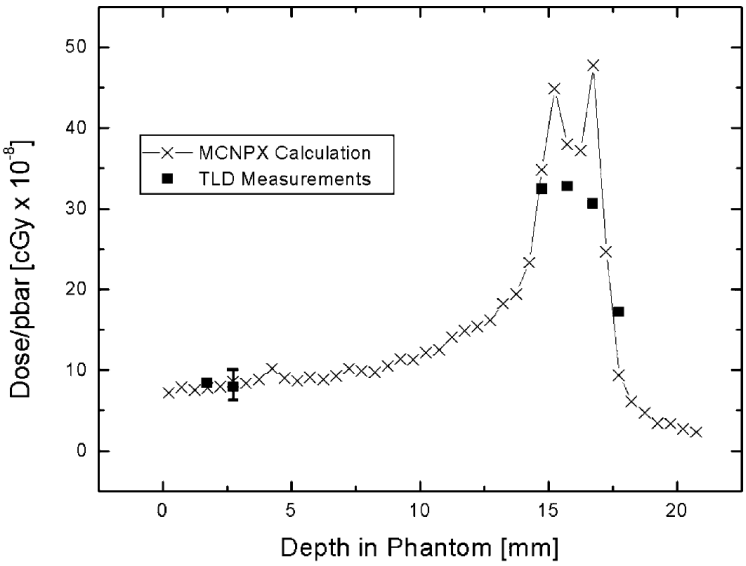

Figure 6.1: Comparison between Monte Carlo (MCNPX) calculations of the depth dose profile of antiprotons to direct measurements using thermoluminescent detector (TLD) chips placed inside a phantom.

calculation it follows that about 1.7 $\times 10^6$ antiprotons would deliver 70 Gy to the peak region. This indicates that for clinical applications it will be necessary to either put the detectors closer to the patient or to use a large surface to get high enough statistics for reconstruction.

A simulation was carried out with detectors with better resolution. Improved performance was clear for reconstruction in the beam direction, however for the transverse beam profile the difference was hard to spot.

The conclusion is that from simulations the idea of real time imaging seems feasible. However a reconstruction of very narrow peaks is unprecise with the methods mentioned above. To reconstruct the width of such peaks, more sophisticated methods would be needed. The inspiration can be found in other imaging methods like computer tomography.

Appendix A

Program for the reconstruction

The program for the reconstruction is written in C++ programming language and was compiled using a Mingw GCC compiler. The source and executable files can be found on *http://cquark.fjfi.cvut.cz/∼ejf/Projekty.html*.

At the beginning of the program the constants describing the geometry of the setup are defined: distances of the detectors from the origin of the coordinate system, size and number of pixels. The coordinate system is right handed as in GEANT4, the origin is located at the beam axis which is identified with the z-axis. The target size is defined with its maximal and minimal coordinates.

The input files are given in the following format:

```
3       1399        303
4       2465        150
5       1362        298
3       1483        276
4       2278        138
```

where the columns correspond to the detector, the row and column number. Numbering of the detectors and pixels is shown in the figure A.1. Details can be easily changed in the file ReadInput.cpp. After reading the input the scanning method in each direction is performed. The important parameters can be set in the main method. These are the width of slices in the scanning method (parameter Increment) and the maximal and minimal target coordinates. They can be set smaller than they are in reality in order to avoid as many fake tracks as possible.

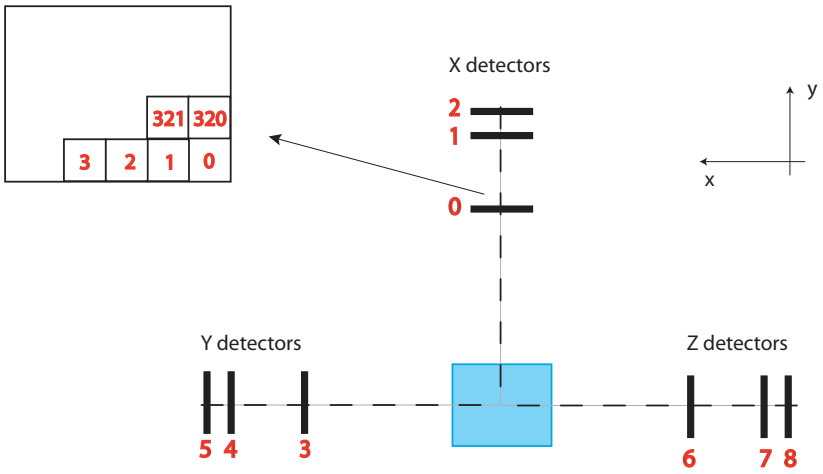

Figure A.1: Numbering of the detectors in an input file.

Bibliography

Agazaryan, N. et al. (2003), 'Status report on experiment AD-4/ACE, Biological effectiveness of antiproton annihilation', *CERN-SPSC-2003-031* .

Agostinelli, S. et al. (2003), 'Geant4 - a simulation toolkit', *Nuclear Instruments and Methods A* **506**, 250–303.

Amado, R., Cannata, F., Dedonder, J., Locher, M. and Shao, B. (1994), 'Coherent pion radiation from nucleon-antinucleon annihilation', *Physical review letters* **72**(7), 970–972.

Amsler, C. (1998), 'Proton-antiproton annihilation and meson spectroscopy with the crystal barrel', *Reviews of modern physics* **70**(4), 1293–1339.

Amsler, C. and Myhrer, F. (1991), 'Low energy aniproton physics', *Annual review of nuclear and particle science* **41**, 219–267.

Belochitskii, P., Eriksson, T. and Maury, S. (2004), 'The CERN antiproton decelerator (ad) in 2002: status, progress and machine development results', *Nuclear instruments and methods in physics research section b-beam interactions with materials and atoms* **214**, 176–180.

Degtyarenko, P., Kossov, M. and Wellisch, H.-P. (2000), 'Chiral invariant phase space event generator III. Modeling of real and virtual photon interactions with nuclei below pion production threshold', *European physical journal, A* **9**(3), 421–424.

Eidelman, S. et al. (2004), 'Review of particle physics 2004', *Physics Letters B* **5892**, 1–1109.

Gray, L. and Kalogeropoulos, T. (1984), 'Possible biomedical applications of antiproton beams: Focused radiation transfer', *Radiation Research* **97**, 246–252.

Holzscheiter, M. (2004), 'Status report on experiment AD-4, Biological effectiveness of antiprotons', *CERN-SPSC-2004-031* .

Holzscheiter, M. (2005), 'Status report on future plans for experiment AD-4, Biological effectiveness of antiproton annihilation', *CERN-SPSC-2005-037* .

Holzscheiter, M. et al. (2004), 'Biological effectiveness of antiproton annihilation', *Nuclear instruments and methods in physics research B* **221**, 210–214.

Horn, D. and Silver, R. (1970), 'Distributions of charged pions', *Physical review D* **2**(9), 2082–2084.

Klempt, E., Batty, C. and Richard, J.-M. (2005), 'The antinucleon–nucleon interaction at low energy: Annihilation dynamics', *Physics reports* **413**, 197–317.

Kossov, M. (2005), 'Simulation of antiproton-nuclear annihilation at rest', *IEEE transactions on nuclear science* **52**(6), 2832–2835.

Kraft, G. (2000), 'Tumor therapy with heavy charged particles', *Progress in particle and nuclear physics* **45**, 473–544.

Weber, U., Becher, W. and Kraft, G. (2000), 'Depth scanning for a conformal ion beam treatment of deep seated tumours', *Physics in medicine and biology* **45**(12), 3627–3641.

Wilson, R. (1946), 'Radiological use of fast protons', *Radiology* **47**, 487–491.